이학박사 학위논문

Artificial Sensory System with High Reliability for Investigation on Food Spoilage

음식물 부패도 연구를 위한 높은 신뢰도를 갖는 인공 감각 시스템

2017 년 8 월

서울대학교 대학원

생물물리 및 화학생물학과

김 대 산

Artificial Sensory System with High Reliability for Investigation on Food Spoilage

지도 교수 전 헌 수

(공동 지도 교수 홍 승 훈)

이 논문을 이학박사 학위논문으로 제출함

2017 년 8 월

서울대학교 대학원

생물물리 및 화학생물학과

김 대 산

김대산의 이학박사 학위논문을 인준함

2017 년 8 월

위 원 장 홍 승 훈 (인)

부위원장 전 헌 수 (인)

위 원 홍 성 철 (인)

위 원 박 혜 윤 (인)

위 원 이 민 백 (인)

Artificial Sensory System with High Reliability for Investigation on Food Spoilage

by

Daesan Kim

Supervised by

Professor Heonsu Jeon

A Dissertation Submitted to the Faculty of Seoul National University in Partial Fulfillment of the Requirements for the Degree of Doctor of Philosophy

August 2017

Department of Biophysics and Chemical Biology

Graduate School

Seoul National University

Abstract

Artificial Sensory System with High Reliability for Investigation on Food Spoilage

Daesan Kim

Department of Biophysics and Chemical Biology

The Graduate School

Seoul National University

An artificial sensor based on nanomaterials has been great interest in research on artificial sensory systems because of their excellent sensitivity and selectivity. The fundamental studies of mammalian sensory systems and the hybridization of bio- and nanomaterials are necessary for the development of the remarkable performance of sensors.

In this dissertation, we have investigated on the activity of various sensory receptor proteins and related responses. Furthermore, we developed artificial sensory systems for the assessment of food quality with high reliability which could mimic the response of mammalian sensory system.

First, we have developed a multiplexed bioelectronics sensor (MBS) that could distinguish various odorants and tastants indicating the food contaminations. We demonstrated that the MBS could monitor the responses of various sensory receptors, showing different binding characteristics. The MBS exhibited a human-like performance in a mixture solution of various target molecules of receptors with 1 pM detection limit. In addition, our sensor platform could recognize food contamination indicators from the real food samples *via* the combinations of responses of different receptors.

Moreover, we developed a highly-stable and oriented nanodiscs (NDs)-based bioelectronic nose (ONBN) for the detection of CV. TAAR13c-embedded nanodiscs (T13NDs) were constructed with TAAR13c produced in *E. coli*. High-quality T13NDs efficiently mimic native binding pockets and lead highly sensitive and selective detections of CV. Here, the immobilization of T13NDs with a desired orientation on floating electrodes *via* linker molecules enabled the active binding site to recognize target molecules, which results in high sensitivity and selectivity of our sensor platform. In addition, an ONBN quantitatively detect CV in real food samples by spoilage periods. These results indicate that our ONBN platform based on GPCR-conjugated FET is a new method for the detection of death-associated odor and has a

potential on practical bioelectronic sensor applications.

Additionally, in the last part of this dissertation, we discussed about the control of enzymatic reaction via nanostructured conducting polymer. We reported a novel bio-chip strategy for control of enzymatic reaction in real-time *via* electrical stimuli. This technique is named as a "bio-switch chip" (BSC). We fabricated BSC structures using polypyrrole (Ppy) with entrapped glucose oxidase (GOx) and showed the switching performance of enzymatic reaction in real-time. The introduction of a negative bias voltage on the BSC structure resulted in the 20-folds increased glucose oxidation reaction than that without a bias voltage. Furthermore, we could control the enzymatic reaction on specific regions because the BSC structures could be fabricated on specific regions. In consideration of the fact that enzymes enable useful and versatile to bio-chemical reactions, the capability to control the enzymatic reactions using simple electrical signals could open up various applications in the field of biochips and biochemical industries.

Keywords: artificial nose, food quality, receptor, nanodisc, carbon nanotube

Student Number: 2011-24029

Table of contents

List of figures

Chapter 1

Introduction

1.1 Carbon Nanotubes

Carbon nanotubes are allotropes of carbon with a nanostructure that can have a length-to-diameter ratio greater than 1,000,000 times. These cylindrical carbon molecules have novel properties that make them potentially useful in many applications in nanotechnology, electronics, optics and other fields of materials science. They exhibit extraordinary strength and unique electrical properties, and are efficient conductors of heat. Nanotubes are categorized as single-walled carbon nanotubes, double-walled carbon nanotubes and multi-walled carbon nanotubes.

The nature of the bonding of a nanotube is described by applied quantum chemistry, specifically, orbital hybridization. The chemical bonding of nanotubes is composed entirely of sp^2 bonds, similar to those of graphite. This bonding structure, which is stronger than the sp^3 bonds found in diamond, provides the molecules with their unique strength. Nanotubes naturally align themselves into "ropes" held together by Van der Waals forces. Under high pressure, nanotubes can merge together, trading some sp^2 bonds for sp^3 bonds, giving the possibility of producing strong, unlimited-length wires through high-pressure nanotube linking. A CNT is a honeycomb lattice rolled into a cylinder [1]. The diameter of a CNT is of nanometer size and the length

of the nanotube can be more than 1 μm.

The structure of swCNT is specified by the chiral vector **OA**, $\mathbf{C_h}$. In figure 1-1 **OB** is the direction of nanotube axis and the **OA** direction corresponds to the nanotubes equator. The $\mathbf{a_1}$ and $\mathbf{a_2}$ in the figure are unit vectors, which are composed of the chiral vector,

(1) $$\mathbf{C_h} = n\mathbf{a_1} + m\mathbf{a_2} \ (0 < m < n)$$

Here n and m are integers. The θ is the angle between chiral vector and one unit vector, which is defined as chiral angle,

(2) $$\Theta = \tan^{-1}\left(\frac{\sqrt{3}m}{2n+m}\right)$$

During the formation of swCNT, the graphite sheet rolls up along the chiral vector $\mathbf{C_h}$. And diameter of swCNT is defined as,

(3) $$d_t = \frac{\sqrt{3}a_{C-C}}{\pi}\sqrt{n^2+m^2+nm} = \frac{\left|\vec{C}\right|}{\pi}$$

Based on the difference between n and m values in the chiral vector, the electronic properties of swCNT can be predicted. If n - m is an integer multiple of three, then the swCNT is metallic tube. Otherwise tube is semiconducting. Also based on the n and m, we can geometrically define three types of swCNT. If n equals to m, then we call it an armchair tube;

if m equals to zero, then we call it a zig-zag tube; otherwise, we call the tube a chiral tube (Figure 1-1). Armchair tube is always a metallic, zig-zag and chiral tubes can be metallic or semiconducting.[1]

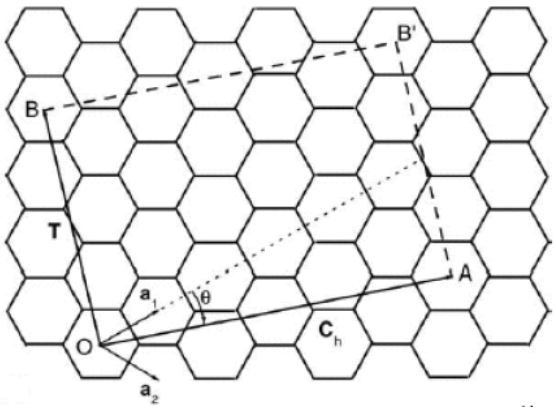

Figure 1-1 The structure of carbon nanotube.[1]

CNT has a couple of important physical properties. CNTs are the strongest and stiffest materials on earth, in terms of tensile strength and Young's modulus respectively.[2] This strength results from the covalent sp^2 bonds formed between the individual carbon atoms. In year 2000, a multi-walled carbon nanotube was tested to have a tensile strength of 63 GPa. In theory, metallic nanotubes can have an electrical current density more than 1,000 times greater than metals such as silver and copper.[3] And all nanotubes are expected to be very good thermal conductors along the tube,[4] exhibiting a property known as "ballistic conduction," but good insulators laterally to the tube axis. It is predicted that carbon nanotubes will be able to transmit up to 6000 W/m per kelvin at room temperature. The temperature stability of carbon nanotubes is estimated to be up to 2800 ℃ in vacuum and about 750 ℃

in air.

1.2 G protein-coupled receptor

GPCRs are integral membrane proteins that have seven transmembrane helices and involved in various physiological processes including cell signal transduction, sensory signaling, neuronal transmission and hormonal signaling.[5] Because of the physiological importance, more than 50% of all drugs target GPCRs and control their activities.[6] The human genome contains about 800 GPCRs and many of these are involved in sensory mechanisms including olfaction and gustation.[7] There are non-sensory human GPCRs known as receptors which are activated by native or endogenous ligands but 143 orphan receptors are not yet known their functions.[7]

The molecular insights of GPCRs were initiated with the cloning of the first mammalian GPCR, β2 adrenergic receptor63 and the crystal structure of rhodopsin64 and β2 adrenergic receptor.[8, 9] The GPCR sequences are conserved at the amino acid level on seven distinct hydrophobic transmembrane regions (each is 20–30 amino acids in length), an extracellular N-terminus and an intracellular C-terminus. According to the conservation and function of GPCRs, they can be classically divided into three main classes, class A (rhodopsin-like)

receptors, which are involved in 85% of the GPCR genes, class B (secretin-like) receptors and class C (metabotropic receptor-like) receptors.

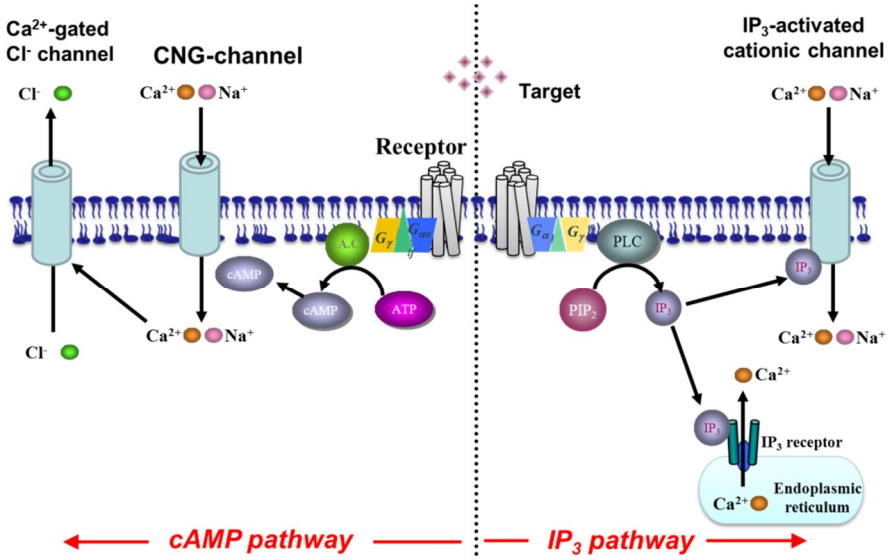

Figure 1-2 Schematic diagram of GPCR-mediated intracellular signal transduction depends on the type of G protein.

There are two major signal transduction pathways involving GPCRs: the cyclic adenosine monophosphate (cAMP) path way and inositol (1,4,5) trisphosphate (IP_3) path way (Figure 1-2).[10] When the specific ligand binds to the GPCR, it causes a conformational change in the receptor, which allows G protein. G protein's α subunit is then dissociated to downstream intracellular signaling proteins or target

functional proteins.

The downstream signal transduction depends on the type of G protein coupled with GPCR (Figure 1-2). Gαs mediates cAMP signal pathway. The enzyme, adenylate cyclase, can be activated by a Gαs and exchanges ATP to cAMP. A cyclic-nucleotide-gated (CNG) channel, finally, is opened and leads to an influx of intracellular Ca^{2+} and Na^{+}. The influx of positive ions depolarizes the ciliary membrane and elicits the generation of potential on the axon. The cAMP also binds to the regulatory subunits and causes the dissociation of the regulatory subunits. This dissociation mediated by cAMP activates protein kinase A and further biological effects can be occurred.

In case of IP_3 path way, the signal transduction is mediated by Gαq. The $G_{\alpha q}$, dissociated by conformational change of the GPCR, activates phospholipase C on the plasma membrane and the lipase hydrolyzes IP_3. The increase IP_3 activates ion channels in the plasma membrane and endoplasmic reticulum.

1.3 Theoretical Modeling for Bio Sensors

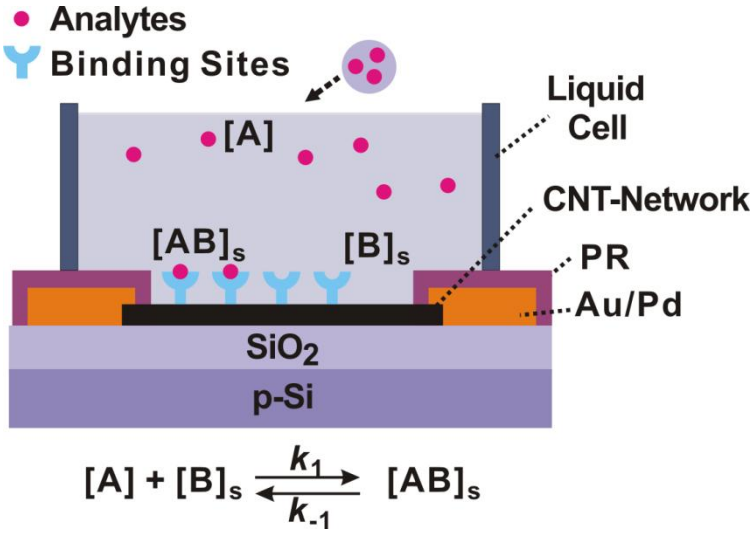

Figure 1-3 Schematic diagram showing the measurement set-up. A CNT channel is connected by source and drain electrodes. The electrodes are covered with photoresist (PR) to prevent electrochemical reactions. A liquid cell is formed to confine the solution. For the theoretical model, we assumed that analytes of bulk concentration $[A]$ get adsorbed on CNT surface with binding sites with surface concentration $[B]_s$. The concentration of adsorbed analytes on CNT surface is $[AB]_s$. The analytes in bulk solution are in equilibrium with those adsorbed on CNT surface.

Figure 1-3 shows the schematic for the theoretical model for the CNT network-based sensors. A CNT channel is connected by source and drain electrodes. The electrodes are covered with photoresist (PR) to prevent electrochemical reactions. A liquid cell is formed to confine the solution. For the theoretical model, we assumed that analytes of bulk

concentration $[A]$ get adsorbed on CNT surface with binding sites with surface concentration $[B]_s$. The concentration of adsorbed analytes on CNT surface is $[AB]_s$. First, we assumed that CNT channels had a finite number of binding sites for analyte molecules, and analytes in bulk solution and those adsorbed on the CNT surface form a Hill equation like

$$[AB]_s = [B]_s \cdot \frac{[A]^n}{[A]^n + 1/K^n} \quad (4)$$

where $[A]$, $[B]_s$, $[AB]_s$, and K represent analyte concentration in bulk solution, binding site concentration on CNT surface, concentration of adsorbed analytes on CNT surface and the equilibrium constant, respectively.

Previous report shows that charge carriers can transport ballistically in individual CNTs. However, CNT network-based channels are usually comprised of multiple CNTs overlapping on each other. In this case, we can expect more diffusive charge transport due to the short mean free paths. Thus, we can ignore any coherent gating effect and assume that the current change ΔI in the channel is linearly proportional to the adsorbed analyte concentration $[AB]_s$ on CNT surfaces like

$$\Delta I = G_L \cdot \Delta V_A \approx g_L V_{ds} \cdot \frac{\Delta q_A}{C_0} = g_L V_{ds} \cdot \frac{q_A [AB]_s}{C_0} = g_L V_{ds} \cdot \frac{q_A}{C_0} [B]_s \cdot \frac{[A]^n}{[A]^n + 1/K^n} \quad (5)$$

where ΔV_A, Δq_A, q_A, C_0 represent the liquid potential change around the CNTs caused by the adsorbed analyte molecules, total electric charge contributed by the adsorbed analyte molecules to the CNTs, electric charge contributed by unit concentration of the adsorbed analyte molecules to the CNTs, and the coupling capacitance due to the analytes. Therefore, the sensor response, defined as the conductance change ($\Delta G=\Delta I/V_{ds}$) with respect to initial conductance G_0, becomes

$$\frac{\Delta G}{G_0} = \left(\frac{g_L}{G_0}\right) \cdot \frac{q_A}{C_0}[B]_s \cdot \frac{[A]^n}{[A]^n + 1/K^n} \tag{6}$$

It is worth mentioning several important aspects of this equation. Firstly, represents the electrical characteristics of a specific CNT junction and should be independent of analyte species. It can be estimated by simple electrical measurement on the CNT devices. Secondly, and K represent the capacitative coupling and adsorption properties of specific analyte molecules onto CNT-based sensor surfaces, respectively. Thus, they should be determined by the analyte type and do not depend on the structures of the CNT devices.

1.4 References

1. Saito, R.; Dresselhaus, G.; Dresselhaus, M. S., *Physical Properties of Carbon Nanotubes*. Imperial College Press: 1998.

2. Yu, M.-F.; Files, B. S.; Arepalli, S.; Ruoff, R. S., Tensile Loading of Ropes of Single Wall Carbon Nanotubes and their Mechanical Properties. *Physical Review Letters* **2000,** *84* (24), 5552-5555.

3. Wei, B. Q.; Vajtai, R.; Ajayan, P. M., Reliability and current carrying capacity of carbon nanotubes. *Applied Physics Letters* **2001,** *79* (8), 1172-1174.

4. Hone, J., Phonons and Thermal Properties of Carbon Nanotubes. In *Carbon Nanotubes: Synthesis, Structure, Properties, and Applications*, Dresselhaus, M. S.; Dresselhaus, G.; Avouris, P., Eds. Springer Berlin Heidelberg: Berlin, Heidelberg, 2001; pp 273-286.

5. Bockaert, J.; Philippe Pin, J., Molecular tinkering of G protein□ coupled receptors: an evolutionary success. *The EMBO Journal* **1999,** *18* (7), 1723-1729.

6. Fang, Y.; Lahiri, J.; Picard, L., G protein-coupled receptor microarrays for drug discovery. *Drug Discovery Today* **2003,** *8* (16), 755-761.

7. Jacoby, E.; Bouhelal, R.; Gerspacher, M.; Seuwen, K., The 7 TM G-Protein-Coupled Receptor Target Family. *ChemMedChem* **2006,** *1* (8), 760-782.

8. Cui, Y.; Lieber, C. M., Functional Nanoscale Electronic Devices Assembled Using Silicon Nanowire Building Blocks. *Science* **2001,** *291* (5505), 851-853.

9. Cherezov, V.; Rosenbaum, D. M.; Hanson, M. A.; Rasmussen, S. G. F.; Thian, F. S.; Kobilka, T. S.; Choi, H.-J.; Kuhn, P.; Weis, W. I.; Kobilka, B. K.; Stevens, R. C., High-Resolution Crystal Structure of an Engineered Human β₂-Adrenergic G Protein–Coupled Receptor. *Science* **2007,** *318* (5854), 1258-1265.

10. Williams, C.; Hill, S. J., GPCR Signaling: Understanding the Pathway to Successful Drug Discovery. In *G Protein-Coupled Receptors in Drug Discovery*, Leifert, W. R., Ed. Humana Press: Totowa, NJ, 2009; pp 39-50.

Chapter 2

Multiplexed Bioelectronic Sensor for Assessment of Food Quality

2.1 Introduction

To overcome the limitations of conventional analytical methods, highly sensitive and selective bioelectronic sensors that mimics the human olfactory/taste system have been reported.[1-3] The sensors used olfactory or taste receptors as a primary recognition molecule and nanomaterials such as a carbon nanotube,[4-15] conducting polymer[16,17] and graphene[18,19] as secondary transducers for the amplification of signal from the primary recognition molecule. The sensors have advantages of their high selectivity of nature system and high sensitivity of a nanomaterial-based electronic sensor. It can be applied in food quality analysis,[8,10,13,14,17] disease diagnosis[11] and environmental assessment.[15]

Although the sensors distinguish their target molecules with high resolution, they could not recognize complex mixtures like humans perceive. The human olfactory and taste system are activated by the combinatorial pattern recognition of various receptors.[20-22] For an accurate representation of the human olfactory/taste system and simultaneous analysis of various odor and taste, multiplexed sensing systems are required with different kinds of receptors. In the previous works, the size of the sensor was small enough, but the size of the measurement equipment was too large for the on-site analysis. Thus, in

addition to multiplexed sensing, miniaturization of the current monitoring system is necessary for practical applications of the bioelectronic sensor.

Herein we report a portable and multiplexed bioelectronic sensor that combines human olfactory and taste receptor with multi-type carbon nanotube (CNT) field-effect transistor (FET) and applied the device for the monitoring of food freshness for the first time. For the multiplexed analysis of taste and odor-causing compounds produced from food, four different kinds of receptors were produced in *E. coli*[23] and their native structures and functional properties were evaluated. And then they were immobilized onto CNT channels with a uniform orientation by nickel-histidine reaction. The CNT-FET sensor was designed in 4x4 multi-channel type and all channels were divided by microwells fabricated by 3D printing technology. For on-site applications, a portable current monitoring system was customized for the multi-channel type bioelectronic sensor and was operated with a power supplied by a laptop computer. The device successfully distinguished the four different molecules, and the pattern recognition of complex mixtures was available without interference in binding of target molecule to its specific receptor by other molecules allowing successful analysis of various food quality.

2.2 Construction of Multiplexed Bioelectronic Sensor

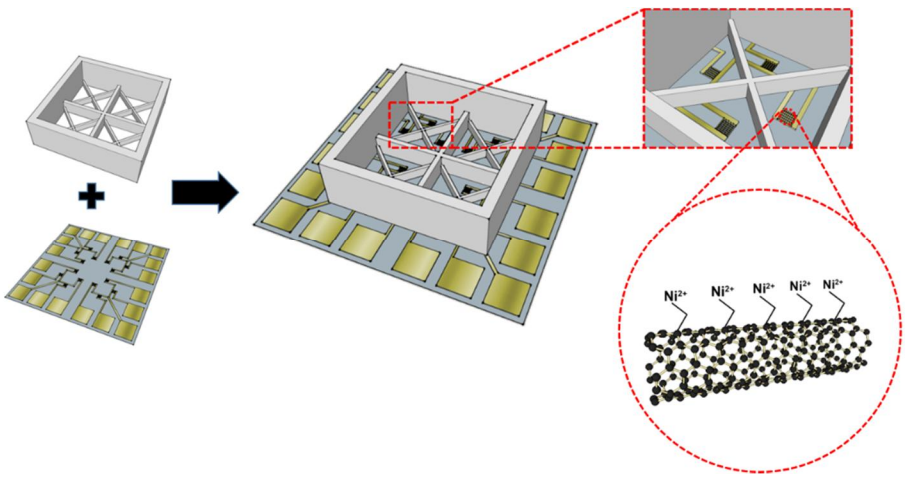

Figure 2-1 Schematic diagram depicting the construction of multiplexed bioelectronic sensor functionalized with nickel ion on CNT channels for the immobilization of human olfactory and taste receptors.

Figure 2-1 shows the schematic diagram representing the fabrication process of a multi-channel sensor (MCS) and channel splitter. The MCS was fabricated with the following method previously reported (detailed in Materials and Methods).[6,9,11] The electrodes and channels were patterned on a SiO_2 wafer via the photolithography method and the patterned wafer was incubated in the SWCNT solution. The passivation layer was made on the electrodes to prevent the leakage of current under the aquatic condition. The fabricated MCS had four quadrant parts and each part composed of four compartmentalized

CNT network channels. The CNT network channels were functionalized with Ni component for immobilization of four types of receptors with the method reported in previous papers.[5,34] The MCSs were incubated in 4-carboxybenzene diazonium tetrafluoroborate solution to to functionalize the SWCNTs on the channels. Then, the carboxylic acid of the 4-carboxybenzene was activated in activation buffer solution and was immersed in Nα,Nα-bis(carboxymethyl)-L-lysine hydrate (NTA-NH_2) solution. Finally, the MCSs were washed with deionized water and were placed in a solution of $NiCl_2$ for functionalization of Ni^{2+} on SWCNTs.

A channel splitter was fabricated using a 3D printer and designed as the different height of walls to prevent various solutions from mixing each other. The wall inside the quadrant part (X-shaped walls) plays a role in splitting the inner part of the MCSs. It prevents one receptor solution from mixing with other receptor solution during receptor immobilization process. The wall has played a role in block affecting one receptor to other quadrant part for the immobilization processes. The outer wall helps to set the consistent volume solutions on the channel parts and block the solution from contacting the pads. The channel splitter was coated with thin layer of polydimethylsiloxane (PDMS) to prevent the leakage of solutions, and was fixed on the

channel part of the MCS. The assembled MCS was baked at 120 °C for 30 min to cure PDMS.

2.3 Characterization of Human Olfactory and Taste Receptors

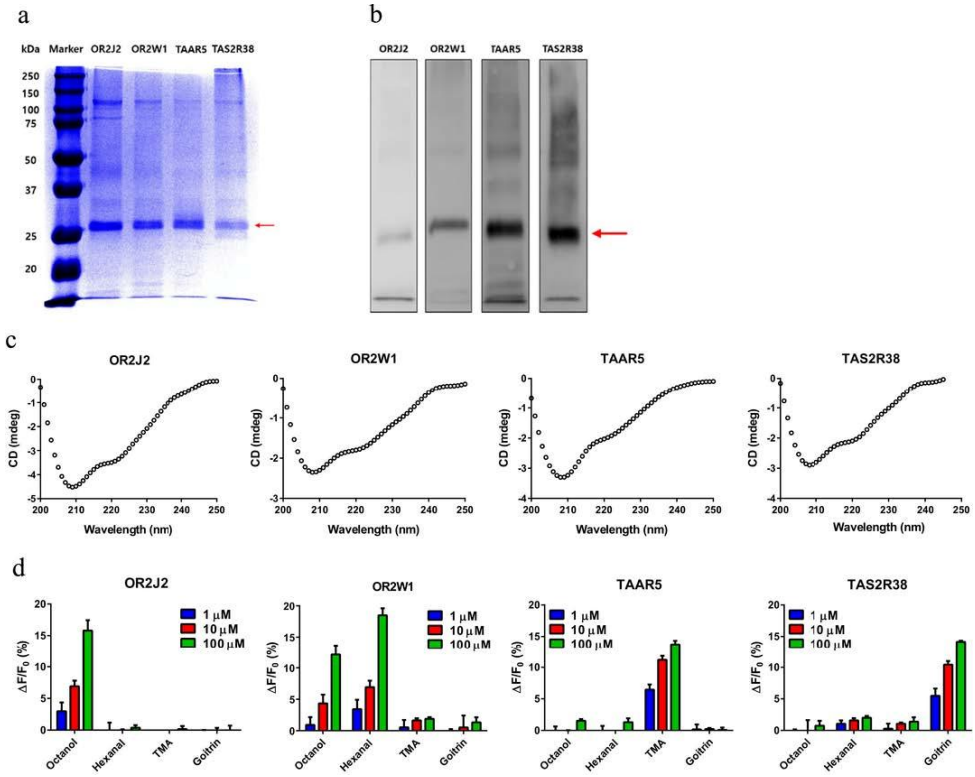

Figure 2-2 Functional production of human olfactory and taste receptors. (a) SDS-PAGE and (b) Western blot analysis of purified and reconstituted receptor proteins; olfactory receptor – OR2J2, OR2W1 and TAAR5, taste receptor – TAS2R38. (c) Secondary structure analysis of olfactory and taste receptor proteins. (d) Evaluation of the receptor selectivity with octanol, hexanal, trymetylamine and goitrin. Error bars, SD, three replicates.

Figure 2-2 (a) shows the SDS-PAGE images of the produced and purified proteins. All receptor proteins were successfully expressed with the expected size and purified with high purity. Western blot was

carried out using his-tag antibody to confirm the fusion of receptor proteins with his-tag (Figure 2-2 (b)). Their secondary structures were analyzed by circular dichroism spectroscopy. Human olfactory and taste receptors are mainly composed by alpha helices and possess strong negative bands at 208 and 220 nm of wavelength.[23,31,32] Figure 1c shows all reconstituted proteins have minimal values at the predicted both wavelengths indicating that they were well-constructed with our reconstitution methods. The functionality of proteins was evaluated using a tryptophan fluorescence quenching method (Figure 2-2 (d)). Mainly, the fluorescence of proteins forming folded structure is due to the excitation of tryptophan residues of the proteins and the conformational change of the proteins by ligand binding decreases the fluorescence intensity by shielding tryptophan residues of the proteins.[33] In this study, the selected sensory proteins contain several tryptophan residues; five residues in OR2J2, three residues in OR2W1, eight residues in TAAR5, and nine residues in TAS2R38. Figure 1d shows that the receptor proteins selectively recognize their ligands with dose-dependent manner.

2.4 Operation of MBS Device

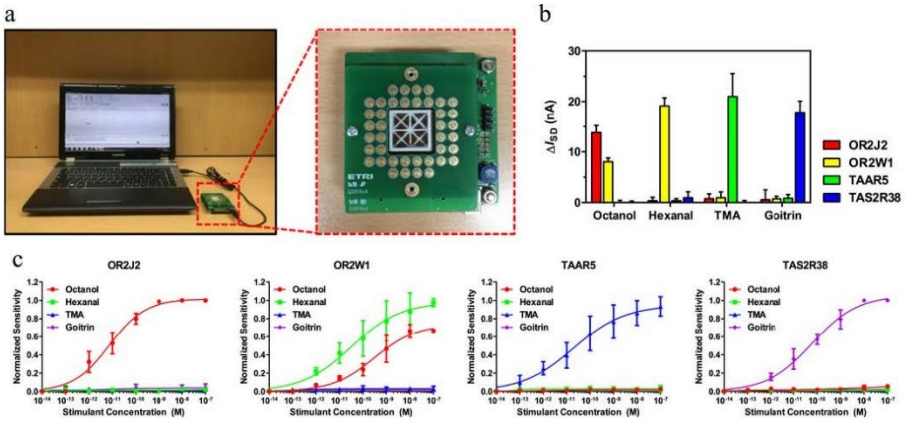

Figure 2-3 Detection of target molecules using customized monitoring platform. (a) A picture of the portable and multiplexed bioelectronic sensor connected to a laptop. (b) Signal pattern recognition of each odor and taste molecules by the bioelectronic sensor (the concentrations of target molecules were fixed at 1 nM). (c) Normalized sensitivity of the sensor based on each sensory receptor.

We also developed a customized portable measurement system for the detection of various molecules using the MCSs (Figure 2-3 (a)). The portable system is composed of 20 probes, a 16-to-1 multiplexer and a microcontroller unit to control the switching from a channel to another one. HyperTerminal was used for the platform of the instrument control. We applied bias voltages of 0.1 V to the reference pads and measured the current signals with the resolution of 10^{-10} A. 16 probes were utilized for the measurement of conductance changes, and

the other 4 probes were used for the reference pads. The channels were switched sequentially from 1 to 16 and repeated 3 times. This platform was designed to connect it to a laptop using a USB cable for its portable application. When odor and taste molecules were injected into the multi-channel type CNT, the receptor-functionalized channel showed the conductance changes with high selectivity (Figure 2-3 (b)), although there were no significant changes in conductance at the pristine CNT channels. The conductance change was normalized to the maximum response and Figure 3c shows the normalized sensitivity and the distinction ability of the sensor at different concentrations of specific target molecules. The dose-dependent signals were analyzed with the Langmuir isotherm and the calculated K_d value was 7.529 x 10^{12} M^{-1} for OR2J2 and octanol, 3.046 x 10^{10} M^{-1} for OR2W1 and octanol, 2.309 x 10^{11} M^{-1} for OR2W1 and hexanol, 1.974 x 10^{11} M^{-1} for TAAR5 and trimethylamine, and 1.782 x 10^{12} M^{-1} for TAS2R38 and goitrin. The human olfactory system is known to recognize a smell by the sum of the receptor binding codes and antagonistic interactions of olfactory receptors were reported.[35] Thus, interference effects between the receptors and odor molecules were evaluated. When we compared electrical signals of each target molecules and the target molecule in mixtures, other molecules in mixture did not affect the electric signal of

target molecule and intrinsic signals of single compounds were measured in the mixtures. These results show that the target molecule in complex mixture can be detected selectively without any interference in binding of target molecule to its specific receptor by other molecules.

2.5 Assessment of Food Freshness Using Bioelectronic Sensor

Food is the major source for human nutrition to maintain their healthy life. Everyone does not want to take stale food and even consumption of contaminated food can lead to serious diseases, and therefore, it is important to control food quality in various food industries.[36] There have been many conventional methods for the assessment of food quality. They are physical (viscosity, chromaticity, turbidity, solubility) method, physicochemical (moisture, acid value, sugar contents, nutritional contents analysis) method, microbiological challenge (bacterial counts) method, and human sensory test (appearance, flavor, taste, texture).[37] However, those methods are not suitable for rapid analysis due to their invasive and complex pretreatment steps, long analytical times and requirements for an expert. To overcome the limitations of the conventional methods, we applied

our bioelectronic sensor for the assessment of food quality. Since our target molecules, such as octanol, hexanal, trimethylamine, and goitrin, are known as indicators of food contamination, it was expected to detect these molecules in various kind of foods and therefore we measured the response of the bioelectronic sensor to the treatment of several food samples. Various food samples were kept in refrigerator until seven days and were used for applying to bioelectronic sensor every day (Figure 2-4). Among the prepared food samples, banana, chicken, potato and strawberry did not induce any significant changes in current of the sensor. However, when beef and pork samples, which were stored in refrigerator for three days, were treated to the OR2J2-functionalized channel, significant changes in current were found and also the changes in current started to be found at the OR2W1-functionalized channel by the treatment of beef and pork after the storage of six and seven days in a refrigerator, respectively. These signals were estimated as a notice by the existence and the concentration change of an odor molecule, octanol in beef and pork. In case of cheese and milk, octanol concentration increased two days after. Trimethylamine began to be detected from both oyster and shrimp at day one and day three, respectively. Goitrin, which is an antithyroid toxin, was found in broccoli and cabbage. Interestingly, the signal

intensity induced by broccoli and cabbage did not increase with increasing storage time and was steadily maintained from day zero to day seven. These results indicate that our sensor can be effectively used for simultaneous analysis of various food freshness and also can replace the complex and time-consuming conventional analytical methods.

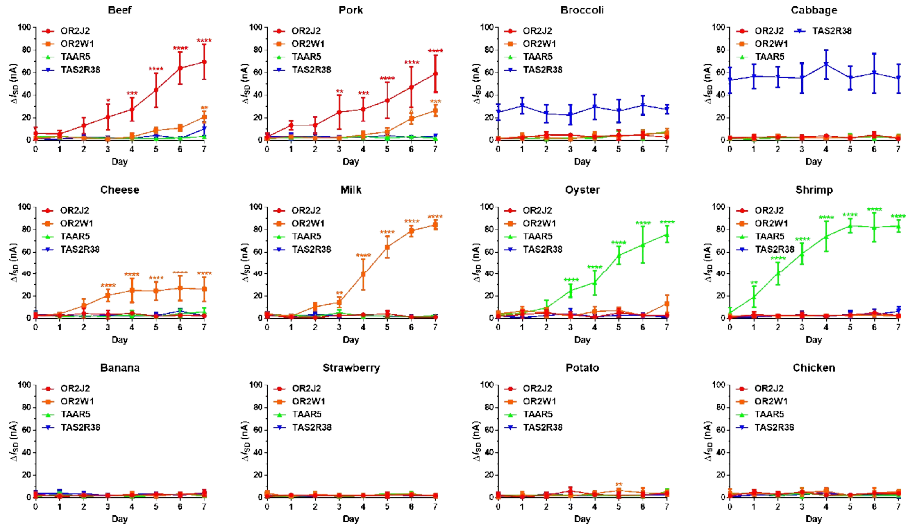

Figure 2-4 Signal pattern analysis of various food samples. Error bars, SD, three replicates. (*$P < 0.05$, **$P < 0.01$, ***$P < 0.001$, ****$P < 0.0001$)

2.6 Conclusions

Olfactory and taste system are well known as a great natural sensing system, and olfactory/taste receptors play an important role in discriminating target odor/taste molecules from a myriad of other

odor/taste molecules. In this study, by the integration of human olfactory/taste receptors to the multi-channel CNT-FET platform with channel splitter, we developed a portable and multiplexed bioelectronic sensor for the simultaneous detection of the target molecule in the mixtures. The sensing device selectively distinguished mixtures of these molecules as well as individual odor and taste molecules with high sensitivity and became portable by combining the miniaturized current measurement system with the carbon nanotube so that electrical signals can be rapidly analyzed in the field and also in real-time. From our results, it is expected that this multiplexed bioelectronic sensor can be used as a useful tool for the quality assessment of various foods and also can be used for diverse on-site detection of various molecules by applying other olfactory and taste receptors to this sensing platform.

2.7 References

1. Glatz, R.; Bailey-Hill, K. Mimicking Nature's Noses: From Receptor Deorphaning to Olfactory Biosensing. *Prog. Neurobiol.* **2011**, 93, 270-296.

2. Stitzel, S. E.; Aernecke, M. J.; Walt, D. R. Artificial Noses. *Annu. Rev. Biomed. Eng.* **2011**, 13, 1-25.

3. Du, L.; Wu, C.; Liu, Q.; Huang, L.; Wang, P. Recent Advances in Olfactory Receptor-Based Biosensors. *Biosens. Bioelectron.* **2013**, 42, 570-580.

4. Kim, T. H.; Lee, S. H.; Lee, J.; Song, H. S.; Oh, E. H.; Park, T. H.; Hong, S. Single-Carbon-Atomic Resolution Detection of Odorant Molecules Using a Human Olfactory Receptor-Based Bioelectronic Nose. *Adv. Mat.* **2009**, 21, 91-94.

5. Goldsmith, B. R.; Mitala, J. J.; Josue, J.; Castro, A.; Lerner, M. B.; Bayburt, T. H.; Khamis, S. M.; Jones, R. A.; Brand, J. G.; Sligar, S. G.; Luetje, C. W.; Gelperin, A.; Rhodes, P. A.; Discher, B. M.; Johnson, A. T. Biomimetic Chemical Sensors Using Nanoelectronic Readout of Olfactory Receptor Proteins. *ACS Nano* **2011**, 6, 5408-5416.

6. Kim, T. H.; Song, H. S.; Jin, H. J.; Lee, S. H.; Namgung, S.; Kim, U. K.; Park, T. H.; Hong, S. "Bioelectronic Super-Taster" Device Based on Taste Receptor-Carbon Nanotube Hybrid Structures. *Lab Chip* **2011**, 13, 2262-2267.

7. Lee, S. H.; Kwon, O. S.; Song, H. S.; Park, S. J.; Sung, J. H.; Jang, J.; Park, T. H. Mimicking the Human Smell Sensing Mechanism with an Artificial Nose Platform. *Biomaterials* **2012**, 33, 1722-1729.

8. Park, J.; Lim, J. H.; Jin, H. J.; Namgung, S.; Lee, S. H.; Park, T. H.; Hong, S. A Bioelectronic Sensor Based on Canine Olfactory Nanovesicle-Carbon Nanotube Hybrid Structures for the Fast Assessment of Food Quality. *Analyst* **2012**, 137, 3249-3254.

9. Jin, H. J.; Lee, S. H.; Kim, T. H.; Park, J.; Song, H. S.; Park, T. H.; Hong, S. Nanovesicle-Based Bioelectronic Nose Platform Mimicking Human Olfactory Signal Transduction. *Biosens. Bioelectron.* **2012,** 35, 335-341.

10. Lim, J. H.; Park, J.; Ahn, J. H.; Jin, H. J.; Hong, S.; Park, T. H. A Peptide Receptor-Based Bioelectronic Nose for the Real-Time Determination of Seafood Quality. *Biosen. Bioelectron.* **2013**, 39, 244-249.

11. Lim, J. H.; Park, J.; Oh, E. H.; Ko, H. J.; Hong, S.; Park, T. H. Nanovesicle-Based Bioelectronic Nose for the Diagnosis of Lung Cancer from Human Blood. *Adv. Healthc. Mater.* **2014**, 3, 360-366.

12. Song, H. S.; Jin, H. J.; Ahn, S. R.; Kim, D.; Lee, S. H.; Kim, U. K.; Simons, C. T.; Hong, S.; Park, T. H. Bioelectronic Tongue Using Heterodimeric Human Taste Receptor for the Discrimination of Sweetners with Human-Like Performance. *ACS Nano* **2014**, 8, 9781-9789.

13. Ahn, J. H.; Lim, J. H.; Park, J; Oh, E. H.; Son, M.; Hong, S.; Park, T. H. Screening of Target-Specific Olfactory Receptor and Development of Olfactory Biosensor for the Assessment of Fungal Contamination in Grain. *Sens. Actuators B Chem.* **2015**, 210, 9-16.

14. Lee, S. H.; Lim J. H.; Park, J.; Hong, S.; Park, T. H. Bioelectronic Nose Combined with a Microfluidic system for the Detection of Gaseous Trimethylamine. *Biosen. Bioelectron.* **2015**, 71, 179-185.

15. Son M.; Cho, D. G.; Lim, J. H.; Park, J.; Hong, S.; Ko, H. J.; Park, T. H.; Real-Time Monitoring of Geosmin and 2-Methylisoborneol, Representative Odor Compounds in Water Pollution Using Bioelectronic Nose with Human-Like Performance. *Biosen. Bioelectron.* **2015**, 74, 199-206.

16. Yoon, H.; Lee, S. H.; Kwon, O. S.; Song, H. S.; Oh, E. H.; Park, T. H.; Jang, J. Polypyrrole Nanotubes Conjugated with Human Olfactory Receptors: High-Performance Transducers for FET-Type

Bioelectronic Noses. *Angew. Chem. Int. Ed.* **2009**, 48, 2755-2758.

17. Song, H. S.; Kwon, O. S.; Lee, S. H.; Park, S. J.; Kim, U. K.; Jang, J.; Park, T. H. Human Taste Receptor-Functionalized Field Effect Transistor as a Human-Like Nanobioelectronic Tongue. *Nano Lett.* **2013**, 13, 172-178

18. Park, S. J.; Kwon, O. S.; Lee, S. H.; Song, H. S.; Park, T. H.; Jang, J. Ultrasensitive Flexible Graphene Based Field-Effect Transistor (FET)-Type Bioelectronic Nose. *Nano Lett.* **2012**, 12, 5082-5090.

19. Kwon, O. S.; Song, H. S.; Park, S. J.; Lee, S. H.; An, J. H.; Park, J. W.; Yang, H.; Yoon, H.; Bae, J.; Park, T. H.; Jang, J. An Ultrasensitive, Selective, Multiplexed Superbioelectronic Nose that Mimics the Human Sense of Smell. *Nano Lett.*, **2015**, 15, 6559–6567.

20. Malnic, B.; Hirono, J.; Sato, T.; Buck, L. B. Combinatorial Receptor Codes for Odors. *Cell* **1999**, 96, 713-723.

21. Firestein, S. How the Olfactory System Makes Sense of Scents. *Nature* **2001**, 413, 211-218.

22. Zou, Z.; Buck, L. B. Combinatorial Effects of Odorant Mixes in Olfactory Cortex. *Science* **2006**, 311, 1477-1481.

23. Yang, H. H.; Song, H. S.; Ahn, S. R.; Park, T. H. Purification and Functional Reconstitution of Human Olfactory Receptor Expressed in Escherichia coli. *Biotechnol. Bioproc. E.* **2015**, 20, 423-430.

24. Saito, H.; Chi, Q.; Zhuang, H.; Matsunami, H.; Mainland, J. D. Odor Coding by a Mammalian Receptor Repertoire. *Sci. Signal.* **2009**, 2, ra9.

25. Wallrabenstein, I.; Kuklan, J.; Weber, L.; Zborala, S.; Werner, M.; Altmuller, J.; Becker, C.; Schmidt, A.; Hatt, H.,; Hummel, T.; Gisselmann, G. Human Trace Amine-Associated Receptor TAAR5 Can Be Activated by Trimethylamine. *PLOS One* **2013**, 8, e54950.

26. Wooding, S.; Gunn, H.; Ramos, P.; Thalmann, S.; Xing, C.; Meyerhof, W. Genetics and Bitter Taste Responses to Goitrin, a Plant Toxin Found in Vegetables. *Chem. Senses* **2010**, 35, 685-692.

27. Tait, E.; Perry, J. D.; Stanforth, S. P.; Dean, J. R. Identification of Volatile Organic Compounds Produced by Bacteria Using HS-SPME-GC-MS. *J. Chromatogr. Sci.* **2014**, 52, 363-373.

28. Marsili, R. T. Comparison of Solid-Phase Microextraction and Dynamic Headspace Methods for the Gas Chromatographic-Mass Spectrometric Analysis of Light-Induced Lipid Oxidation Products in Milk. *J. Chromatogr. Sci.* **1999**, 37, 17-23.

29. Hedegaard, R. V.; Kristensen, D.; Nielsen, J. H.; Frost, M. B.; Ostdal, H.; Hermansen, J. E.; Kroger-Ohlsen, M.; Skibsted, L. H. Comparison of Descriptive Sensory Analysis and Chemical Analysis for Oxidative Changes in Milk. *J. Diary Sci.* **2006**, 89, 495-504.

30. Dalgaard, P.; Madsen, H. L.; Samieian, N.; Emborg, J. Biogenic Amine Formation and Microbial Spoilage in Chilled Garfish (Belone Belone Belone) – Effect of Modified Atmosphere Packaging and Previous Frozen Storage. *J. Appl. Microbiol.* **2006**, 101, 80-95.

31. Kiefer, H.; Kriefer, J.; Olszewski, J. D.; Von Heijne, G.; Prestwich, G. D.; Breer, H. Expression of an Olfactory Receptor in Escherichia coli: Purification, Reconstitution, and Ligand Binding. *Biochemistry* **1996**, 35, 16077-16084.

32. Kaiser, L.; Graveland-Bikker, J.; Steuerwald, D.; Vanberghem, M.; Herlihy, K.; Zhang, S. Efficient Cell-Free Production of Olfactory Receptors: Detergent Optimization, Structure, and Ligand Binding Analyses. *Proc. Natl. Acad. Sci. U. S. A.* **2008**, 105, 15726-15731.

33. Vivian, J. T.; Callis, P. R. Mechanisms of Tryptophan Fluorescence Shifts in Proteins. *Biophys. J.* **2001**, 80, 2093-2109.

34. Graff, R. A.; Swanson, T. M.; Strano, M. S. Synthesis of Nickel-Nitrilotriacetic Acid Coupled Single-Walled Carbon Nanotubes for

Directed Self-Assembly with Polyhistidine-Tagged Proteins. *Chem. Mater.* **2008**, 20, 1824-1829.

35. Oka, Y.; Omura, M.; Kataoka, H.; Touhara, K. Olfactory Receptor Antagonism Between Odorants. *EMBO J.* **2004**, 23, 120-126.

36. Hammond, R. A.; Dube, L. A Systems Science Perspective and Transdisciplinary Models for Food and Nutrition. *Proc. Natl. Acad. Sci. U. S. A.* **2012**, 109, 12356-12363.

37. Peri, C. The Universe of Food Quality. *Food Qual. Prefer.* **2006**, 17, 3-8.

Chapter 3

Nanodisc-based Bioelectronic Sensor for Assessment of Food Quality

3.1 Introduction

G protein-coupled receptors (GPCRs) play important roles in the cellular responses of the human body. Thus, they are significantly involved in many human diseases and are the target of approximately 40% of all modern medicinal drugs.[1, 2] Trace amine-associated receptors (TAARs), a class of GPCR, are conventional amine receptors binding to endogenous compounds structurally related to classical biogenic amines. It has been reported that trace amine-associated receptor 13c (TAAR13c) in the zebrafish (*Danio rerio*) functions as an olfactory receptor (OR) and has an efficient specificity to the death-associated odor cadaverine (CV).[3-6] CV, generated by bacterial decarboxylation of lysine, is an extremely repulsive odor to humans, among various biogenic amines. In addition, CV is one of the important markers for decayed foods because various kinds of food products contain lysine. Therefore, it has been suggested that the detection of CV can be applied to various fields of industrial applications and scientific investigations.[3, 7]

For the production of recombinant proteins, the *Escherichia coli* (*E. coli*) has been widely used as a host cell because of its great advantage in productivity and convenience. However, the production of

GPCR in *E. coli* remains a challenge because of their strong hydrophobicity, a complicated charge distribution and membrane inserting mechanism of bacterial cells.[8-10] Among many reconstitution techniques of receptors, nanodiscs (NDs) have been considered the most appropriate tool for GPCR reconstitution.[11, 12] NDs are composed of a receptor, a lipid bilayer and membrane scaffold proteins (MSPs), which tightly wrap the edge of the a lipid bilayer, thus NDs can be stable in an aqueous environment[10, 12-14] and mimic the native structure of the receptor in a cell.[13, 14] An ND-based biosensor using Sf9 insect cells has also been reported.[13] However, an ND-based biosensor using an *E. coli* system, which has great advantages in productivity over other systems, has not been previously reported. A carbon nanotube field-effect transistor (CNT-FET) with floating electrodes can exhibit improved performance compared with a conventional CNT-FET.[15, 16] The floating electrode structure on a CNT-FET can enhance the sensitivity of the device *via* the increased effect of Schottky barrier modulation. The Au floating electrodes also have advantages in the functionalization of specific biomolecules on their surfaces. The surfaces of floating electrodes have larger areas than conventional devices as well as more suitable conditions for the functionalization of biomolecules.

Here, we report the development of an oriented nanodisc-functionalized bioelectronic nose (ONBN) using TAAR13c-embedded nanodiscs (T13NDs) with high selectivity and sensitivity for the detection of CV. The T13NDs using receptors produced in *E. coli* enable the immobilized receptor to have stability and a natural binding pocket. Moreover, the T13NDs were immobilized on floating electrodes of a CNT-FET in a desired orientation, which increased the total binding sites of T13NDs. As a result, the ONBN exhibited improved performance in terms of sensitivity and selectivity, as well as reliability and reproducibility. Furthermore, the ONBN could distinguish the target molecules in food samples with differing degrees of spoilage. Our approach can offer a remarkable sensing system toward a practical bioelectronic sensor to enable the detection of death-associated compounds.

3.2 Fabrication of oriented nanodisc-functionalized bioelectronics nose using TAAR13c-embedded nanodiscs

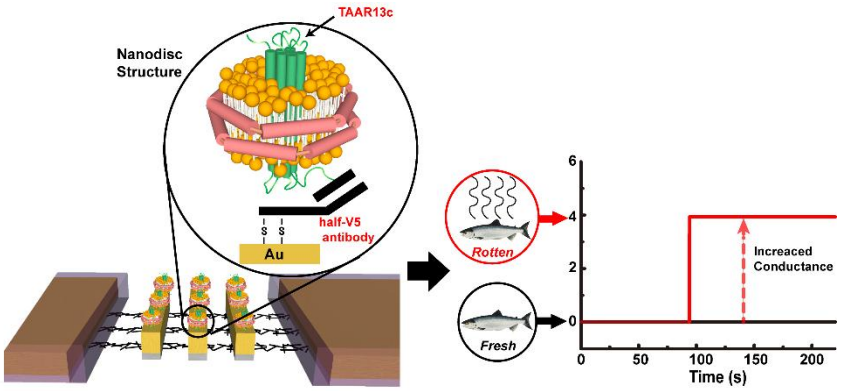

Figure 3-1 Schematic diagram of an ONBN. This illustrates the ONBN and possible sensor response curves of an ONBN. T13NDs were successfully immobilized on floating electrodes of a CNT-FET, which leads to a high-performance ONBN. The ONBN can selectively discriminate the rotten foods from fresh samples.

Figure 3-1 depicts the schematic diagram and the predicable electrical response of an ONBN. A CNT-FET with floating electrodes was fabricated following previously-reported processes. A detailed method is described in Supporting Information. In brief, CNTs were patterned on a SiO_2 substrate as transistor channels, and then, Pd/Au electrodes were fabricated via a thermal evaporation method. Finally, the source and drain electrodes were passivated using photoresist to avoid a leakage current through an aqueous environment. After the

fabrication of the device, T13NDs were immobilized on the Au surfaces of the floating electrodes using half-fragment V5 antibody (Ab) as a linker. Here, V5 epitope at T13NDs binds to the half-fragment V5 Ab on the Au surface, and the immobilized T13NDs on the Au surfaces were oriented along the direction so that the binding pockets of TAAR13c on the device stand upside. In previous works, the devices with randomly immobilized biomolecules also have been studied.[23, 24] But, it could be considered that they have a limitation in capability to bind with. Therefore, ONBNs could provide an ideal method for the detection of the specific target molecules.

3.3 Characterization of TAAR13c expressed in HEK-293 cell and high-quality TAAR13c-embedded nanodiscs

Figure 3-2 (a) shows the experimental results of the dose dependent response of TAA13c expressed in HEK-293 cells. We used a dual-glo luciferase assay system which was suitable for the characterization of the TAAR13c in terms of its selectivity. TAAR13c expressed cells exhibited a significant response to CV, but mock vector transfected cells had no meaningful responses. This supports that TAAR13c was successfully expressed in HEK-293 cells (Figure 3-2 (a)). Figure 3-2 (b) shows the selective responses of TAAR13c with 1

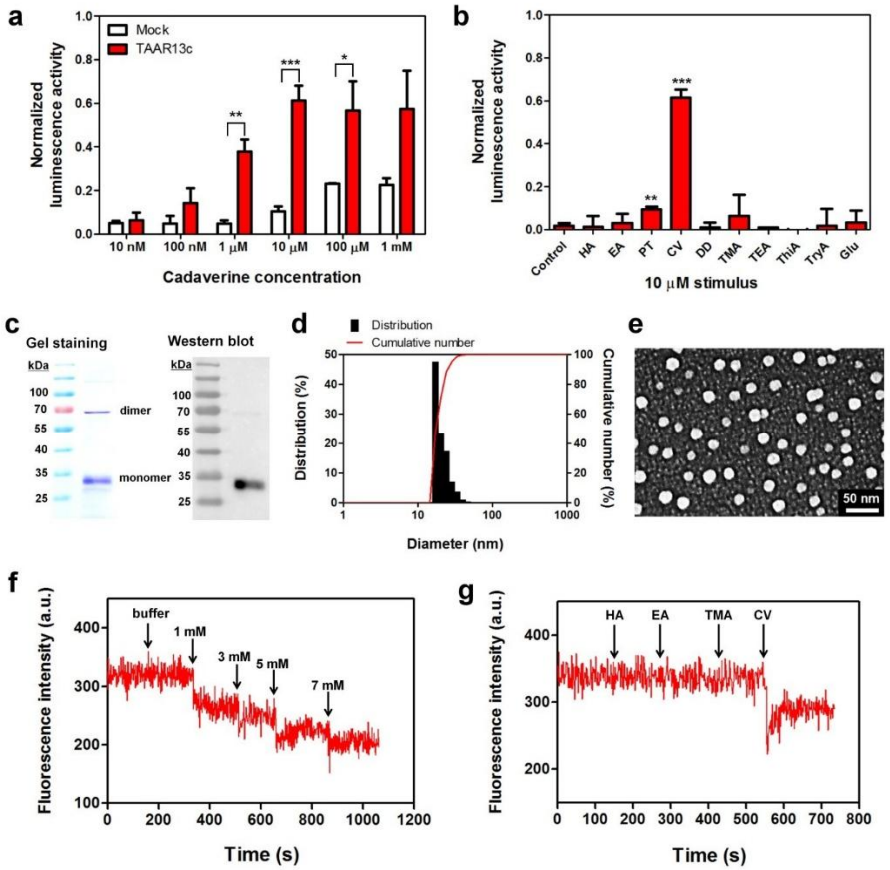

Figure 3-2 Characterization of TAAR13c expressed in HEK-293 cell and high-quality TAAR13c-embedded nanodiscs (T13NDs). The purified TAAR13c in NDs was produced in *E. coli*. (a) Dose-dependent response of TAAR13c to the CV ($^{*}p<0.05$, $^{**}p<0.01$, $^{***}p<0.001$). (b) Selectivity of TAAR13c with various amines (HA, hydroxylamine; EA, ethanolamine; PT, putrescine; CV, cadaverine; DD, diaminodecane; TMA, trimethylamine; TEA, trimethylamine; ThiA, thiamine; TryA, tryptamine; Glu, glutamine). (c) SDS-PAGE analysis of purified TAAR13c produced in *E. coli*. (d) DLS size distribution of optimized T13NDs. (e) FE-SEM image of T13NDs. (f) Real-time tryptophan fluorescence of T13NDs with increasing concentration of the CV. (g) Selective response of T13NDs to CV measured by real-time intrinsic fluorescence.

μM stimulus of various amines. The TAAR13c was co-expressed with RTP1S and $G_{\alpha olf}$, increasing the level of expressions and efficiencies of a signal transduction. The selective binding properties of TAAR13 were investigated using various amines, which had different amine moieties and structures. Our results show TAAR13c responded selectively to CV among various amines. Although PT seems to stimulate the TAAR13c partially, there were no significant responses. The results are consistent with previous reports that the TAAR13c is the most sensitive and selective receptor to death-associated odor CV.[3, 5]

Figure 3-2 (c) shows the gel staining and western blot results of purified TAAR13c expressed in *E. coli*. Toward a receptor-based research, the TAAR13c expressed in *E. coli* was purified with a high purity and applied to the formation of receptor NDs. The purification and functional reconstitution of GPCRs for the development of receptor-based biosensors were reported in our previous studies.[9, 25] For the production of T13NDs, the TAAR13c and lipids were mixed as detergent micelle forms, and then the membrane scaffold protein apolipoprotein A-I (ApoA-I) was added in the mixtures to wrap the lipid/receptor complex. The T13NDs was obtained after the removal of detergent using Bio-bead. The bands of TAAR13c in gel staining

indicate that TAAR13c was purified with a high purity. Moreover, the observed bands were successfully confirmed as TAAR13c by a western blot analysis using V5 epitope Ab. These results show the TAAR13c was prepared with a high quality.

Figure 3-2 (d) shows the DLS measurement of T13NDs. For the assembly of the T13NDs, ApoA-I, the representative membrane scaffold protein, was successfully expressed in *E. coli* and purified with a high purity. After the assembly of the NDs, the NDs-complex solutions were applied to the SEC for the removal of residual unbound proteins. The fraction of T13NDs from the SEC separation was collected and analyzed by DLS. We have tested various conditions for the formation of receptor-NDs (lipid sonication and protein concentration) and found the best choice for the formation of optimized T13NDs. It indicates a quite narrow size distribution with *ca.* 20 nm in its diameter, which is close to the diameter values estimated by FE-SEM images (Figure 3-2 (e)). These results clearly demonstrate that the T13NDs were successfully self-assembled in homogeneous discoidal shapes.

Figure 3-2 (f) shows the tryptophan fluorescence of T13NDs with the increasing concentration of CV in a real time. In order to analyze the affinity of T13NDs with CV, the real-time intrinsic fluorescence of

T13NDs was measured. With the sequential addition of the increasing CV amounts up to 7 mM, the significant fluorescence change of T13NDs was displayed (*ca*. 25%). On the other hand, there was no responses by control buffer solution. Figure2g indicates the selective response of T13NDs with CV in real-time tryptophan fluorescence using various amines which have different structures and amine moieties. It shows that the intrinsic tryptophan fluorescence of T13NDs was significantly quenched only by a stimulus of CV. Many researches have reported that the intrinsic fluorescence of functional receptor was quenched when the ligand selectively binds to the receptor.[9, 26, 27] Therefore, these results show that TAAR13c with a high purity was effectively reconstituted in NDs.

3.4 Characteristics of an oriented NDs-functionalized CNT-FET with floating electrodes

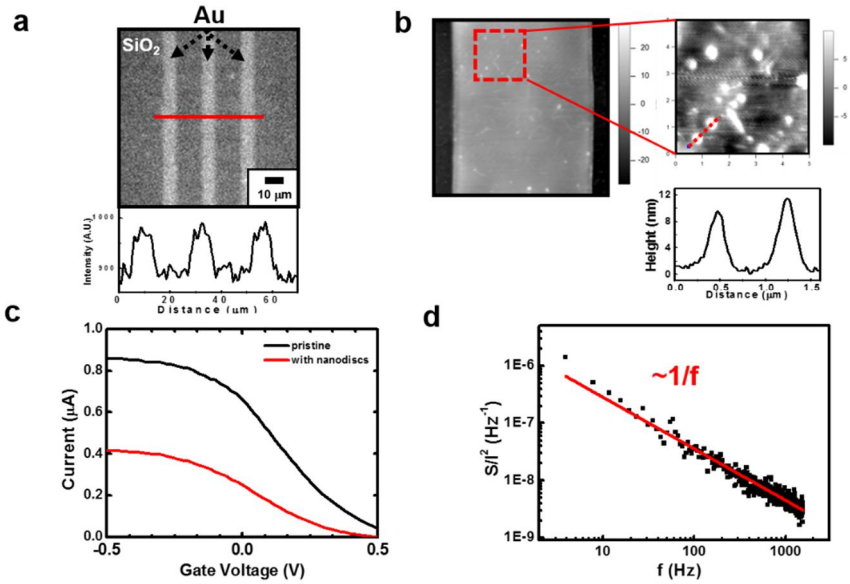

Figure 3-3 Characteristics of an oriented NDs-functionalized CNT-FET with floating electrodes. (a) Fluorescence image and the intensity profile of V5 antibody-functionalized floating electrodes of a CNT-FET. The images represent the functionalized V5 antibody on the floating electrodes of the ONBN. (b) Liquid AFM images and the sectional height profile of an ONBN. The AFM images show the well immobilized-NDs structures on the floating electrode of ONBN. The height graph indicates that the immobilized-NDs had the similar sizes as those reported previously. (c) Gate profiles of ONBNs without or with NDs. These are typical p-type semiconductor characteristics. (d) Electrical noise characteristics of an ONBN at a frequency domain. It exhibited a typical 1/f characteristics.

Figure 3-3 shows the characteristics of an ONBN. Figure 3-3 (a) shows the fluorescence image of V5 Ab-functionalized floating

electrodes and its intensity profile graph. To prepare T13ND layers with a desired orientation, we utilized V5 Ab as linker molecules to attaches T13NDs on floating electrode surfaces. Then, the V5-functionalized Au electrodes were incubated in fluorescence dye-labeled V5 Ab solution (Detailed methods in METHODS section). The fluorescence microscopy was utilized to confirm functionalization of V5 Ab on floating electrodes of the ONBN. The image clearly shows the bright regions corresponding to the floating electrodes functionalized with V5 Ab, while the dark regions are the SiO_2 surfaces. Note that the intensity profile of the Au surface was higher than that of the SiO_2 surface as shown in the intensity profile (bottom of Figure 3a). This result indicates the immobilized V5 Ab with dye molecules on the floating electrode surfaces. This result implies that V5 Ab was successfully immobilized on the floating electrodes.

Figure 3-3 (b) shows the atomic force microscopy (AFM) images of the T13ND-functionalized floating electrode in liquid environments and the height profile graph. The *left* and *right* images were measured in a tapping mode AFM with the scan rates of *0.4* and *0.1* Hz, respectively. The *bright* or *dark* regions correspond to a *T13ND-functionalized floating electrode* or *CNT channels on SiO_2 substrates*. We can find white spots with its height of ~10nm which is comparable to a

previously reported diameter of a T13ND.[10, 12] This result implies the functionalization of T13NDs on the floating electrode.

Figure 3-3 (c) is the gate profile graph of a ONBN before and after the immobilization of T13NDs. The gate profiles exhibited typical p-type semiconductor characteristics in both cases, indicating that the transistor characteristics of the ONBN was maintained even after the immobilization of T13NDs on floating electrodes. Note that the electrical currents were reduced by the immobilization of T13NDs. It is presumably because negatively-charged parts of receptors immobilized on floating electrodes gave the gating effect and affected the drain-source currents.[33]

Figure 3-3 (d) shows the electrical noise characteristics of an ONBN. The data could be fitted by a straight line, indicating a typical 1/f noise behavior. The noise amplitude was found to be ~ 10^{-6} which was similar to the previously-reported values of clean network-based CNT-FETs without T13NDs.[27] These results indicate that the functionalization of T13NDs on our CNT devices did not increase its noise levels, which can be critical in achieving a high sensitivity in our devices.

3.5 Operation of ONBN Device

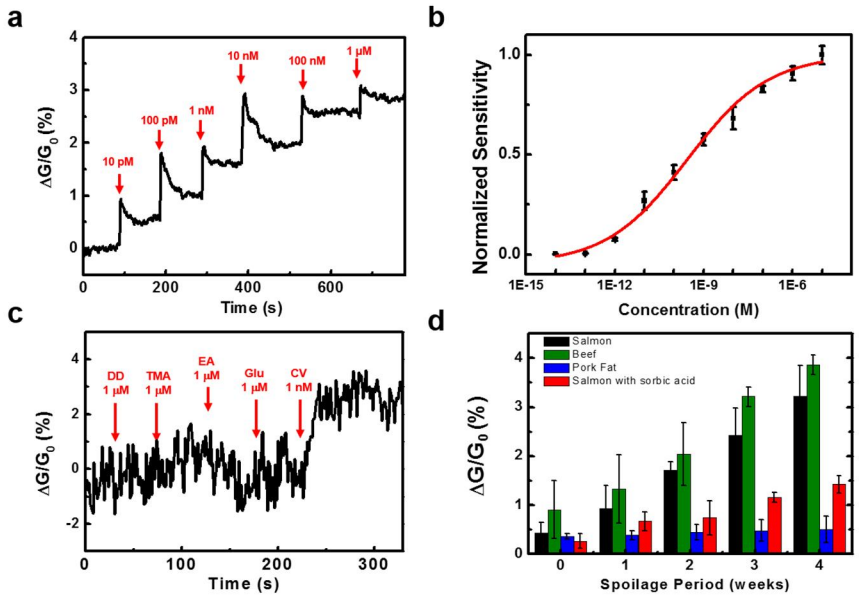

Figure 3-4 Responses of ONBN devices to CV with various conditions. (a) Real-time response of an ONBN to CV with various concentrations. The additions of CV solution induced the increase of conductance of the ONBN in dose-dependent manner. (b) Dose-dependent response curve of the ONBN to CV. By fitting the data using Eq. (3), the equilibrium constant K was estimated as 3.63×10^{11} M^{-1}. (c) Real-time response of an ONBN to various molecular species with amine functional groups. The introduction of non-target molecules caused negligible conductance changes of the ONBN. (d) Comparison of the sensor responses of our ONBN devices to different rotten food samples. As the spoilage period for salmon and beef increased, the ONBN devices exhibited rather large sensor responses.

Figure 3-4 (a) shows the real-time response of an ONBN to

various concentrations of CV. Here, while adding various concentrations of target solutions, we measured drain-source currents of the ONBN using a semiconductor analyzer. The drain-source bias voltage was maintained as 0.1 V during the measurement. Then, the measured data of current changes during the additions of CV were normalized by the original current values to estimate the normalized conductance change $\Delta G/G_0$. Note that the conductance of the ONBN was sharply increased after adding various concentrations of CV solutions. The ONBN exhibited the increase of its conductance by CV solutions with its concentration as low as 10 pM, indicating the high sensitivity of our devices. The plausible mechanism for this response is that the binding of protonated positively-charged CV molecules to TAAR13c increased the work function of the floating electrode.[34] Thus, the binding of CV decreased the Schottky barrier for hole carriers in the device and increased the conductance of the ONBN device.[28]

Figure 3-4 (b) shows the graph for the normalized sensitivity N of ONBNs at different concentrations of CV. The normalized sensitivity was estimated by normalizing the sensor sensitivity ($|\Delta G/G_0|$) with respect to its maximum sensitivity value.[29-32] The measured response curves can be analyzed using the model based on the Langmuir

isotherm theory as previous studies.[35] In this model, the density C_s of CV molecules bound to the T13NDs on an ONBN can be written as

(1) $$C_s = \frac{C_{s\,max} \cdot C}{1/K + C}$$

where C and K represent *the concentration of odorant in a solution* and *an equilibrium constant between odorant and T13NDs*, respectively. $C_{s\,max}$ is the density of T13NDs on the electrodes of an ONBN. The binding events between CV and T13NDs induced the increased conductance. If we assume that a conductance change ΔG is linearly proportional to the number of bounding CV molecules on T13NDs, a sensor sensitivity can be approximated as $|\Delta G/G_0| \sim kC_s$, where k is a constant representing the response characteristics of an ONBN. Therefore, the sensor sensitivity could be written as

(2) $$|\Delta G/G_0| = k\frac{C_{s\,max} \cdot C}{1/K + C}$$

As C becomes very large, the sensor sensitivity $|\Delta G/G_0|$ could converge to $k \cdot C_{s\,max}$. Thus the normalized sensitivity N can be written as

(3) $$N = \frac{C}{1/K + C}$$

By fitting the measured data with this model, we could estimate the

equilibrium constant K between T13NDs and CV as 3.63×10^{11} M^{-1}, which is a rather large compared with previously-reported values measured using cells or biological systems. This result implies that our ONBN device can detect target CV molecules with a much higher sensitivity than cells or biological systems.

Figure 3-4 (c) shows the real-time response of an ONBN to various molecules containing amine functional groups. Here, we injected DD, TMA, EA, Glu and CV molecules to the ONBN in series while measuring the sensor responses. DD and EA have the similar structures with CV, TMA is a fishy odor, and Glu is one of amino acids. The structures of these molecules are presented in Supporting Information. Note that, the ONBN device exhibited negligible sensor responses to non-target molecules with a rather high concentration of 1 μM. However, the conductance of the ONBN increased sharply by adding CV with a concentration of 1 nM which is 1000 times lower concentration than that of non-target molecular species. This result clearly shows that our ONBN can selectively detect CV with a very low concentration even with various other molecular species with a high concentration.

Figure 3-4 (d) shows the responses of ONBNs to various real sample solutions obtained from rotten foods. Each tested food sample was prepared in HEPES buffer solution and filtered by ultrafiltration membranes. The detailed method is in the METHODS section. The samples from salmon and beef with a longer spoilage period exhibited larger sensor responses. On the other hand, the samples from salmon with sorbic acid, one of the preservatives, exhibited decreased sensor responses, presumably due to the reduced spoilage of the salmon by sorbic acid. It indicates that our ONBN devices can be used to evaluate the quality of real food samples *quantitatively*. Interestingly, the pork fat sample showed negligible sensor responses even with a large spoilage period. It is presumably because CV, the target of our ONBN device, is the product of a decarboxylation of lysine which existed in salmon and beef at a large quantity, but not in pork fat[36]. These results indicate our ONBN devices can be utilized to evaluate the quality of versatile real food samples quantitatively under complicated environmental conditions.

3.6 Conclusions

In conclusion, we developed a highly-stable NDs-based

bioelectronic nose for the detection of CV. The NDs were successfully constructed with TAAR13c produced in *E. coli*. High-quality T13NDs efficiently mimic native receptors and lead highly sensitive and selective detections of CV. Especially, the immobilization of T13NDs with a desired orientation on floating electrodes via linker molecules enabled the high density of recognition elements and active binding pocket in our ONBN devices, which results in its high sensitivity and selectivity. Furthermore, an ONBN measure CV quantitatively in real food samples with different spoilage periods. These results show that our ONBN device based on high-quality GPCR-conjugated FETs is a novel technique for the detection of death-associated odor and has a great potential toward a practical bioelectronic sensor applications.

3.7 References

1. Siehler, S. *Biotechnology journal*. **2008**, 3, 4.

2. Drews, J. *Science*. **2000**, 287, 5460.

3. Hussain, A.; Saraiva, L. R.; Ferrero, D. M.; Ahuja, G.; Krishna, V. S.; Liberles, S. D.; Korsching, S. I. *Proc Natl Acad Sci U S A*. **2013**, 110, 48.

4. Liberles, S. D. *Ann N Y Acad Sci*. **2009**, 1170, 1.

5. Sharma, K.; Ahuja, G.; Hussain, A.; Balfanz, S.; Baumann, A.; Korsching, S. I. *Sci Rep*. **2016**, 6.

6. Liberles, S. D.; Buck, L. B. *Nature*. **2006**, 442, 7103.

7. Grisshammer, R.; Tate, C. G. *Q Rev Biophys*. **1995**, 28, 3.

8. Gafvelin, G.; von Heijne, G. *Cell*. **1994**, 77, 3.

9. Yang, H.; Song, H.; Ahn, S.; Park, T. H. *Biotechnol Bioproc E*. **2015**, 20, 3.

10. Denisov, I. G.; Sligar, S. G. *Nat Struct Mol Biol*. **2016**, 23, 6.

11. Serebryany, E.; Zhu, G. A.; Yan, E. C. *Biochim Biophys Acta*. **2012**, 1818, 2.

12. Whorton, M. R.; Jastrzebska, B.; Park, P. S.; Fotiadis, D.; Engel, A.; Palczewski, K.; Sunahara, R. K. *J Biol Chem*. **2008**, 283, 7.

13. Ritchie, T.; Grinkova, Y.; Bayburt, T.; Denisov, I.; Zolnerciks, J.; Atkins, W.; Sligar, S. G. *Methods in enzymology*. **2009**, 464.

14. Bayburt, T. H.; Sligar, S. G. *FEBS Lett*. **2010**, 584, 9.

15. Goldsmith, B. R.; Mitala, J. J.; Josue, J.; Castro, A.; Lerner, M. B.; Bayburt, T. H.; Khamis, S. M.; Jones, R. A.; Brand, J. G.; Sligar, S. G.; Luetje, C. W.; Gelperin, A.; Rhodes, P. A.; Discher, B. M.; Johnson, A. T. *ACS Nano*. **2011**, 5, 7.

16. Glück, J. M.; Koenig, B. W.; Willbold, D. *Anal Biochem*. **2011**, 408, 1.

17. Lee, J.; Lee, H.; Kim, T.; Jin, H. J.; Shin, J.; Shin, Y.; Park, S.; Khang, Y.; Hong, S. *Nanotechnology*. **2012**, 23, 8.

18. Lee, M.; Jung, J. W.; Kim, D.; Ahn, Y. J.; Hong, S.; Kwon, H. W. *ACS Nano*. **2015**, 9, 12.

19. Liberles, S. D. *Curr Opin Neurobiol*. **2015**, 34.

20. Liu, C. H. J.; Lu, W. C. *J Chin Inst Chem Eng*. **2007**, 38, 5-6.

21. Pacquit, A.; Lau, K. T.; McLaughlin, H.; Frisby, J.; Quilty, B.; Diamond, D. *Talanta*. **2006**, 69, 2.

22. Liu, S. F.; Petty, A. R.; Sazama, G. T.; Swager, T. M. *Angew Chem Int Ed Engl*. **2015**, 54, 22.

23. Oh, J.; Yoo, G.; Chang, Y. W.; Kim, H. J.; Jose, J.; Kim, E.; Pyun, J. C.; Yoo, K. H. *Biosens Bioelectron*. **2013**, 50.

24. Lo, Y. S.; Nam, D. H.; So, H. M.; Chang, H.; Kim, J. J.; Kim, Y. H.; Lee, J. O. *ACS Nano*. **2009**, 3, 11.

25. Song, H. S.; Lee, S. H.; Oh, E. H.; Park, T. H. *Curr Microbiol*.

2009, 59, 3.

26. Michalke, K.; Huyghe, C.; Lichiere, J.; Graviere, M. E.; Siponen, M.; Sciara, G.; Lepaul, I.; Wagner, R.; Magg, C.; Rudolph, R.; Cambillau, C.; Desmyter, A. *Anal Biochem*. **2010**, 401, 1.

27. Son, M.; Kim, D.; Ko, H. J.; Hong, S.; Park, T. H. *Biosens Bioelectron*. **2017**, 87.

28. Kim, B.; Lee, J.; Namgung, S.; Kim, J.; Park, J. Y.; Lee, M. S.; Hong, S. *Sensor Actuat B-Chem*. **2012**, 169.

29. Kim, T. H.; Song, H. S.; Jin, H. J.; Lee, S. H.; Namgung, S.; Kim, U.-k.; Park, T. H.; Hong, S. *Lab on a Chip*. **2011**, 11, 13.

30. Takagi, S.; Toko, K.; Wada, K.; Ohki, T. *J Pharm Sci*. **2001**, 90, 12.

31. Jin, H. J.; Lee, S. H.; Kim, T. H.; Park, J.; Song, H. S.; Park, T. H.; Hong, S. *Biosens Bioelectron*. **2012**, 35, 1.

32. Kim, T. H.; Lee, S. H.; Lee, J.; Song, H. S.; Oh, E. H.; Park, T. H.; Hong, S. *Advanced Materials*. **2009**, 21, 1.

33. Venkatakrishnan, A. J.; Deupi, X.; Lebon, G.; Tate, C. G.; Schertler, G. F.; Babu, M. M. *Nature*. **2013**, 494, 7436.

34. Sharma, K.; Ahuja, G.; Hussain, A.; Balfanz, S.; Baumann, A.; Korsching, S. I. *Scientific Reports*. **2016**, 6.

35. Patnaik, P.; Dean, J. A. Dean's analytical chemistry handbook. 2nd ed, McGraw-Hill: New York, **2004,** section 13.

36. Pipek, P.; Rohlík, B.; Potůček, T.; Šimoniová, A. *Maso International.* **2012**, 2.

Chapter 4

Other Works: “Bio-switch Chip” based on Nanostructured Conducting Polymer and Entrapped Enzyme

4.1 Introduction

In living systems, various enzyme molecules serve to realize versatile biochemical reactions critical for bio-functionalities. Such enzymes have also been utilized for a wide range of biochip and other biochemical applications.[1-3] For example, in a glucose meter, glucose oxidase (GOx) is coated on the electrode surfaces and used for the measurement of glucose concentrations in solutions. It was also reported that thin layers of polypyrrole (Ppy) polymer with entrapped GOx can be coated on a metal electrode to build highly-efficient glucose sensors[4-7]. DNA polymerase has been utilized to accelerate the duplication of DNAs in polymerase chain reaction (PCR) systems.[8,9] For such biochemical applications based on enzyme, it is often essential to switch on or off the enzymatic reactions via various external control parameters such as temperature controls or chemical treatment. However, previous control methods of enzymatic reactions are often slow and require complicated processes, which have limited the further advances in the enzyme-based biochip applications. On the other hand, polypyrrole (Ppy) polymer structures have been utilized to store chemical species and quickly release them by simple external electrical stimuli so that the released chemical species switch on or off the activity of biomelecules in real-time. For example, nanowires based on

Ppy were used to hold ATP molecules and release it by external electrical potential, allowing one to turn on or off the activity of biomotor proteins in real-time.[10,11] In this case, however, the Ppy polymer structures can store only limited amounts of the chemical species, which can be problematic in some applications such as repeated switching or massive chemical treatments. Various polymer films including Ppy were also utilized as a membrane to separate two solution cells and control the mass transports of versatile small molecules including ions.[12,13] In this case, the mass transport through the membrane can be efficiently controlled via various stimuli such as electrical potential, which shows the possibility of using such polymer films in building advanced nanobio-devices based on the control of biomaterials transport.

We report a switchable bio-chip platform where enzyme molecules were entrapped in expandable conducting polymer electrodes. In this device, GOx enzyme was entrapped in a thick Ppy layer, and the thick Ppy layer was used as a membrane to control the mass transport from the external glucose solution into the trapped GOx enzyme via electrical stimuli so that glucose oxidation reaction in the solution can be turned on or off via simple electrical stimuli. This device structure is

named here as a “bio-switch chip” (BSC) in the sense that it allows one to switch on or off the bio-molecular reactions via electrical stimuli. We found that a negative bias voltage on the Ppy structures in the chips opened up channels for the mass transport of glucose solution into the trapped GOx and enhanced the enzymatic reaction by more than 20 times compared with the case without bias voltages. Furthermore, since the BSC structures could be fabricated on a specific location on a substrate, we could control the enzymatic reaction rate on *localized* regions. Considering that biomolecular enzymes can enable extremely versatile bio-chemical reactions and conducting polymers are known to entrap various biomolecular species without degradation, [10,11,13,14] our strategy can be quite a versatile method and should open up various applications for basic researches and biochemical industries.

4.2 Structure of Bio-switch Chip

Figure 4-1 (a) shows the schematic diagram illustrating the fabrication method of a BSC structure on an Au substrate. The detailed procedure for the fabrication of a bio-switch chip can be found in the Materials and Methods section. Briefly, photoresist (PR) layers were patterned on an Au substrate using a photolithography method. Ppy patterns were deposited on the exposed Au surfaces using an electrochemical deposition method in the solution including GOx enzyme, resulting in Ppy patterns with entrapped GOx only on the exposed Au surface regions. Then, the substrate was rinsed by acetone to remove PR patterns and leave only BSC structures. Here, the photoresist layers should be removed thoroughly because some remaining photoresist layers during the BSC operations with electric bias voltages may cause unexpected contamination in the glucose solution. Since organic solvents can damage biomolecules, the acetone rinsing process could degrade the GOx molecules on the *surface* of Ppy structures.[15,16] However, previous works show that Ppy films could efficiently block the penetration of small molecules including organic solvents and protect the functionality of biomolecules trapped in them.[10-14,17,18] Thus, we expect the GOx trapped *deep inside* the Ppy films was protected by the Ppy films and maintained its functionality.

Note that since we utilized only conventional fabrication methods such as microfabrication and electrochemical deposition techniques, such BSC structures with various shapes can be mass-produced on virtually-general electrode surfaces.

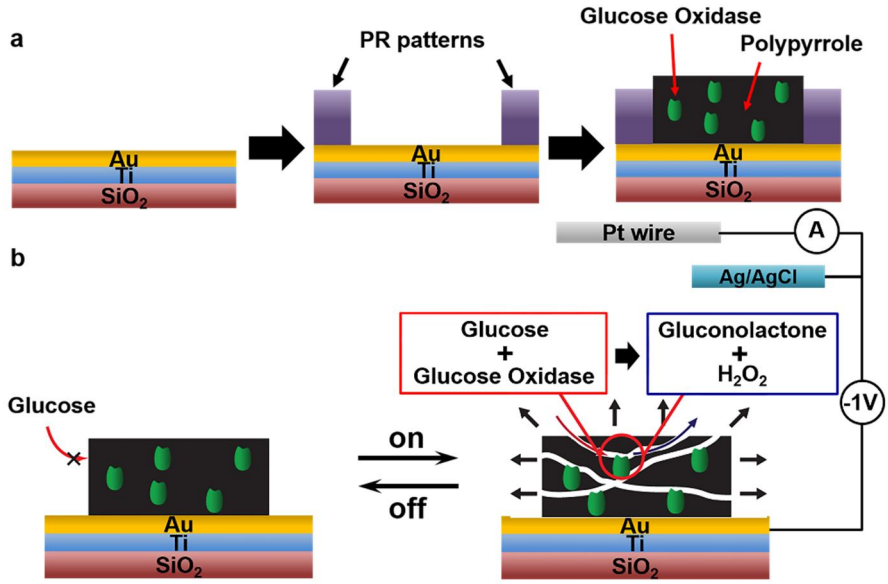

Figure 4-1 (a) Schematic diagram showing the fabrication process for a "bio-switch chip" (BSC). Photoresist layers were patterned on an Au substrate via conventional microfabrication process. Then, Ppy layer was electrodeposited in the solution including GOx so that Ppy layers with entrapped GOx were formed only on exposed Au surfaces. The substrate was rinsed with acetone solution to remove PR layer patterns, leaving only a BSC structure. (b) Schematic diagram showing the operation mechanism of a BSC structure for the real-time control of enzymatic reaction using electrical stimuli. The application of a negative bias voltage of -1 V on the BSC structure resulted in the volume expansion of the BSC structure, which opened up the pathway to

entrapped GOx and enabled the enzymatic reaction on glucose molecules by GOx.

Figure 4-1 (b) shows the basic operation mechanism of a BSC structure in a glucose solution. Without any bias voltage, glucose molecules could hardly react with GOx molecules entrapped inside the BSC structures since they were blocked by Ppy polymer. When a negative bias voltage was applied on the BSC structures through the Au substrate, the nano-structure of Ppy was expanded as reported previously.[19-21] However, the application of a positive bias voltage did not affect the volume change of the BSC structure. Such a volume expansion of the Ppy structures opened up nanoscale holes and provided a pathway for the glucose molecules to flow into the GOx molecules in the BSC structures. Such a voltage-controlled volume expansion of Ppy films has been utilized for various applications based on the mass transport of various chemical and biochemical molecular species.[10,11,13,14] As a result, GOx can catalyze the oxidation of β-D-glucose into D-glucono-δ-lactone and hydrogen peroxide (H_2O_2).[22] The enzymatic reaction could be confirmed by checking the formation of H_2O_2 in the solution using a hydrogen peroxide assay kit.[23,24] When the applied bias voltage was removed, the BSC structures shrank back to

the origin volume and blocked the pathways inside the BSC structures, thus GOx entrapped in BSC structures stopped the enzymatic reactions. Note that such switching steps can be repeated many times over a long time period.

4.3 Characterization of Bio-switch Chip

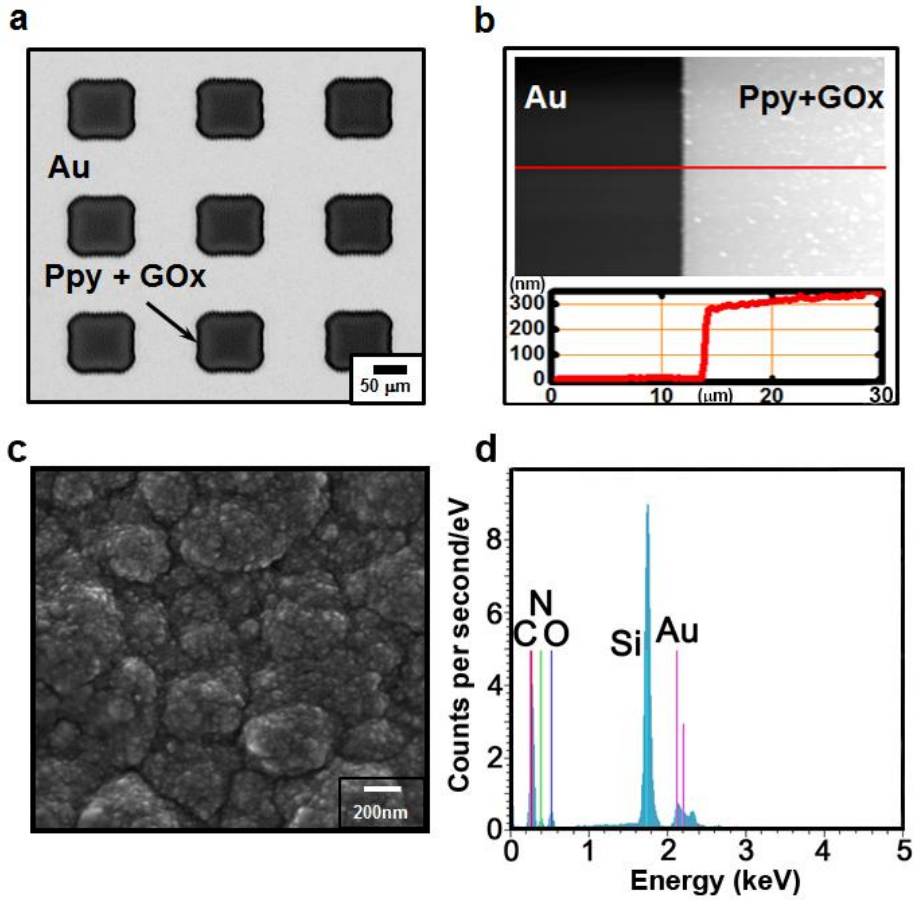

Figure 4-2 Microscopy analysis of BSC structures on Au electrode. (a) Optical microscopy image of a BSC structure array. (b) AFM image and height profile

on the edge of a BSC structure. (c) High resolution SEM image of a BSC surface. (d) EDS results on a BSC surface.

We examined the structure and components of BSCs via various microscopy (Figure 4-2). Figure 4-2 (a) shows the optical microscopy image of the BSC on an Au substrate. The dark and bright regions represent the BSC structures and the Au substrate, respectively. The square patterns of the BSC structures with clean edges were uniformly distributed over the Au substrate. Figure 4-2 (b) shows the atomic force microscopy (AFM) topography image and a cross section on the edge of the BSC structure. This result shows a rather smooth surface with the 300 nm thickness of the BSC structure. These results show that our fabrication method can be utilized to fabricate well-defined BSC structures over a large surface area.

Figure 4-2 (c) shows the high resolution scanning electron microscopy (SEM) image of a BSC structure. The surface of the BSC structure developed nodules on whole region, which was similar to the previously-reported structures of electrodeposited Ppy films.[25] The energy-dispersive X-ray spectroscopy (EDS) analysis on the BSC structure shows the peaks of C, N, and O which are typical elements of Ppy polymer structures (Figure S1d).[26] The peaks of Si and Au came

from the Au film substrate coated on a Si wafer. These results imply that our method can be utilized to fabricate BSC structures with a well-controlled nano-morphology and minimal contaminations.

4.4 Operation of Bio-switch Chip

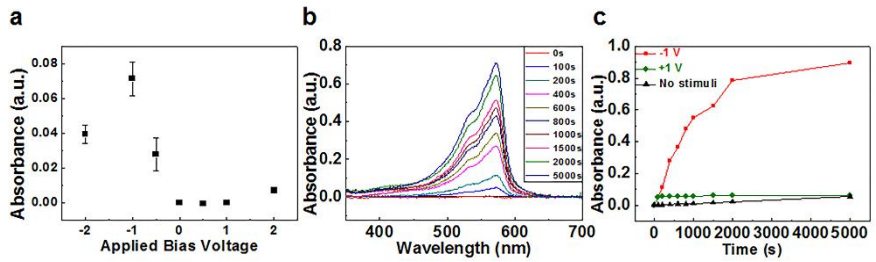

Figure 4-3 Electrical switching operation of BSC structures with entrapped GOx molecules in glucose solution. The BSC structures were turned on by applying a -1 V bias voltage through the Au substrate over a different time period. The enzymatic reaction by the entrapped GOx generated H_2O_2. Thus, the activation of enzymatic reaction was measured by measuring the concentration of generated H_2O_2 via Amplex Red Reagent Assay kit. (a) Absorbance spectra of the glucose solution mixed with Amplex Red reagent (1:1 by volume) after the operation of BSC structures over different time periods. (b) Peak height (at 571 nm) of the absorbance spectra measured from the glucose solution mixed with Amplex Red reagent (1:1 by volume) after the operation of BSC structures for different time periods. The red, green and black marks represent the data taken from the glucose solution oxidized by the BSC structures with the bias voltage of -1 V, +1 V, and 0 V, respectively. (c) Peak height (at 571 nm) of the absorbance spectra measured from the glucose solution mixed with Amplex Red reagent (1:1 by volume) after the operation of BSC structures with different bias voltage for 500 seconds. For each BSC

operation with a specific bias voltage condition, the absorbance peak heights were measured for four solution samples and used to estimate the average values and error bars.

Figure 4-3 shows the operation of BSC structures with entrapped GOx molecules in a glucose solution. The enzymatic reactions by the BSC device were turned on by applying the bias voltage on the BSC device, which generates H_2O_2 as a by-product. When a small amount of the glucose solution was taken and mixed with Amplex Red reagent solution (1:1 by volume) without any bias voltages, the H_2O_2 in the glucose solution reacted with Amplex Red reagent. This reaction produced fluorescent resorufin with a characteristic absorption peak at 571 nm, which could be measured using a spectrophotometer. Thus, we could quantitatively estimate the enzymatic reactions by measuring the concentration of the generated H_2O_2 in the glucose solution via Amplex Red reagent assay kit and a spectrophotometer. Figure 4-3 (a) shows the absorption spectra of the glucose solution mixed with Amplex Red reagent after the BSC operations for different time periods. It shows the characteristic peak of the reaction product, resorufin, at 571 nm. Note that the peak amplitude increased as the operation time of the BSC increased, indicating the electrical stimuli on our BSC structures stimulate the enzymatic

reactions by entrapped GOx molecules and generated H_2O_2. The absorbance data can be utilized to estimate the reaction speed. For example, the glucose solution, after 800 s reaction by the BSC structures, contains the generated H_2O_2 with 25 □M concentration, indicating the average reaction rate of 31 nM/s. Considering that the area of the used BSC structures was $5.6 \times 10^{-4}/m^2$, the reaction rate per unit area of the BSC structure with a bias voltage was 5.54 $nM/(cm^2 \cdot s)$. This value is comparable to the previous reaction rate values of the GOx-coated on Pt electrode.[7] These results show that our BSC structure can be utilized to activate enzymatic reactions via electrical stimuli in real-time.

Figure 4-3 (b) shows the operation of our BSC devices for different time periods. Here, the BSC was turned on for different time periods, and the absorption peak height of the glucose solution mixed with the assay kit was plotted over the different operation times. When -1 V was applied onto the BSC structures, the peak began to increase immediately indicating that the GOx activity was switched on immediately. When the bias voltage of -1 V was maintained over time, the peak (red line) increased almost linearly for the first 800 seconds, indicating very active enzymatic reactions by the entrapped GOx.

However, over a long time period after 800 seconds, glucose in the solution was probably used up, and thus, the increase rate of the absorption peak height slowed down, which is a typical behavior of chemical reactions. On the other hand, when zero (black line) or +1 V (green line) was applied on our BSC structures, the graph shows negligible absorption peak height, indicating the BSC chip was turned off and the enzymatic reaction by the entrapped GOx was blocked efficiently. Note that when the BSC device was turned on by -1 V bias, the enzymatic reaction speed was more than 20 times larger than those data when the device was off. These results clearly show that the enzymatic reactions of GOx inside the BSC could be regulated via electrical stimuli.

Figure 4-3 (c) shows the results after the operation of BSC devices with various bias voltages. The bias voltages were applied onto the BSC structures through the working electrode with respect to the Ag/AgCl reference electrode for 500 seconds. Then, the absorption peak height of the glucose solution mixed with the assay kit was measured. We could observe large absorption peaks from the solution after the operation of BSC devices with *negative* bias voltages, indicating a rapid glucose oxidation at this bias voltage condition. It also should be noted that our BSC devices exhibited very little glucose oxidation

reaction with *zero or positive* bias voltages. Previously, GOx enzyme on the *surface* of various electrodes has been utilized as a part of glucose sensors, where the GOx exhibited rapid glucose oxidation with *zero or positive* bias voltages on the electrode.[4-7] In the case of our BSC devices, GOx can be trapped *on* or *deep inside* a rather thick Ppy films, and that *on the surface* of the Ppy flims could be degraded due to the acetone rinsing process during the device fabrication processes.[15,16] The negligible glucose oxidation reaction by our BSC devices with a *zero* or *positive* bias conditions indicate the GOx on the surface of our Ppy structures was significantly damaged, presumably, due to the acetone treatment during the device fabrication processes. However, the large glucose oxidation reaction at *negative* bias voltages implies that GOx deep inside our thick Ppy structures was protected by the Ppy films during the device fabrication processes and could oxidize glucose when the Ppy films expanded and allowed the external solution to access the GOx at *negative* bias voltage conditions. Previous works show that thick Ppy films with a *zero* bias voltage could block the penetration of small molecules and protected biomolecules trapped in them.[10-14,17,18] On the other hand, at large negative bias voltages like -2 V, the absorption peak height was decreased indicating the reduced concentration of H_2O_2. Presumably, the glucose oxidation speed of our

BSC devices was limited by the limited amount of GOx in the devices, while the generated H_2O_2 by the glucose oxidation reactions could be electrochemically reduced rapidly by a rather high bias voltage on the electrodes.[27,28] These results indicate that the ideal operation condition of our devices was a negative bias voltage up to -1 V on the Ppy structures.

4.5 Control of Enzymatic Reaction *via* Bio-switch Chip

Our method allows one to create BSC structures on a specific region on a solid substrate so that enzymatic reaction only on the region can be controlled (Figure 4-4). As a proof of concept, we fabricated BSC devices containing GOx and pure Ppy structures on the same substrate to demonstrate the localized enzymatic reaction controlled by electrical stimuli (Figure 4-4 (a)). Here, the solutions around two cells were separated by a well to clearly see the effect of localized enzymatic reactions. Detailed fabrication processes can be found in Materials and Method section. In brief, a well was fabricated by 3D printer, and it was coated with polydimethylsiloxane (PDMS) to prevent the leakage of glucose solution. The well was mechanically clamped down on an Au substrate, and Ppy structures were electrodeposited *with* or *without*

entrapped GOx. After the deposition process, each cell was rinsed thoroughly with deionized water. Note that in this cell, we could apply the same bias voltage onto the Ppy structures *with* or *without* entrapped GOx and compare the results of the localized enzymatic reactions under identical conditions.

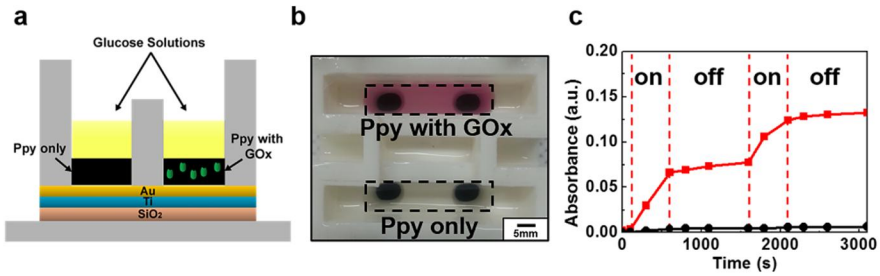

Figure 4-4 Real-time control of enzymatic reactions in localized regions via electrical stimuli. (a) Schematic diagram showing BSC device and pure Ppy structures separated by a well. (b) Optical image showing the glucose solution mixed with Amplex Red reagent around BSC (upper red solution) and pure Ppy (lower transparent solution) structures after the BSC operation. Here, -1 V bias was applied both BSC and Ppy structures for 30 seconds and Amplex Red reagent was added (1:1 by volume) without any bias voltage. The red color came from the resorufin generated by the reaction between Amplex Red reagent and H_2O_2. (c) Peak height of the absorbance spectra measured from the glucose solution mixed with Amplex Red reagent solution after the operation of BSC structures over different time periods. At the on-state, -1 V was applied to the BSC structures, while zero bias was applied to the structures at the off-state.

We filled the cells with the same glucose solution and applied – 1 V on the both sides of the cells for 30 s. Then, the Amplex Red reagent assay

kit was introduced without any bias voltage (Figure 4-4 (b)). The *red* (upper side) or *transparent* (lower side) solution regions in Figure 3b represent the optical image of the solutions around Ppy structures *with* or *without* entrapped GOx molecules in the cells, respectively. The red color in the upper cell came from the resorufin generated by the reaction between Amplex Red reagent and H_2O_2 in the solution. It indicates the active enzymatic reaction by the entrapped GOx generated H_2O_2 as a by-product. On the other hand, the cell of pure Ppy structures did not exhibit a red color, indicating no reaction even with the same bias voltage. These results clearly show that our BSC devices can be utilized to control the enzymatic reactions only on a specific region in the solution.

Our BSC devices can be utilized to switch on or off the enzymatic reactions in real-time. Figure 4-4 (c) shows the peak height of the absorption spectra measured from the glucose solutions after turning on or off a BSC device for different time periods. We applied the negative bias voltage of -1 V on the BSC structures for 500 s (on state) and then removed the bias voltage for 1000 s (off state), which was repeated twice. The absorption peak intensity increased rapidly at 'on state', whereas it did not increase at 'off state' (Figure 3c, red line). Note that when we applied –1 V bias, the absorption peak height began to

increase immediately, indicating the glucose oxidation reaction was switched on immediately by our BSC device. Furthermore, when a bias voltage was removed, the absorption peak height immediately stopped to increase, which shows that our BSC device can switch off the oxidation reaction. These results show that our device can switch on or off the glucose oxidation reaction rapidly via electrical signals. The oxidation reaction speed at the on-state was more than twenty times faster than that at the off-state. On the other hand, the reaction did not occur in the cell with pure Ppy structures without GOx enzyme. It means that the GOx-free BSC do not show any significant reaction by electrical stimuli. We also demonstrated that our BSC device can be repeatedly turned on or off in many cycles (Figure S2 in Supporting Information). These results clearly show that our BSC devices can be utilized to control the enzymatic reaction with both *spatial* and *temporal* resolutions.

4.6 Conclusions

In conclusion, we demonstrated the BSC platforms comprised of GOx enzyme entrapped in thick Ppy polymer layers on Au electrode surface. This device allows one to turn on or off the glucose oxidase

reactions in glucose solution in real time via electrical stimuli. In this chip, we could stimulate the enzymatic reaction on the localized regions by twenty times via electrical stimuli on the BSC chip. Considering that enzymes can provide extremely versatile chemical functionalities which area often critical biological processes, the real-time control capability of our BSC platforms should open up quite versatile applications including advanced biochips and biochemical devices which can be turned on or off via simple electrical signals.

4.7 References

1. Mendoza, L. G.; McQuary, P.; Mongan, A.; Gangadharan, R.; Brignac, S.; Eggers, M., High-throughput Microarray-based Enzyme-linked Immunosorbent Assay ELISA.. *Biotechniques* **1999**, 27, 778-780.

2. Houseman, B. T.; Gawalt, E. S.; Mrksich, M., Maleimide-Functionalized Self-Assembled Monolayers for the Preparation of Peptide and Carbohydrate Biochips†. *Langmuir* **2003**, 19, 1522-1531.

3. Tang, Z. P.; Louie, R. F.; Lee, J. H.; Lee, D. M.; Miller, E. E.; Kost, G. J., Oxygen Effects on Glucose Meter Measurements with Glucose Dehydrogenase- and Oxidase-based Test Strips for Point-of-care testing. *Crit Care Med* **2001**, 29, 1062-1070.

4. Fu, Y.; Li P.; Xie, Q.; Xu, X.; Lei, L.; Chen, C.; Zou, C.; Deng W.; Yao, S., One-Pot Preparation of Polymer–Enzyme–Metallic Nanoparticle Composite Films for High-Performance Biosensing of Glucose and Galactose. *Adv Funct Mater* **2009**, 19, 1784-1791.

5. Chen, C.; Xie, Q.; Yang, D.; Xiao, H.; Fu, Y.; Tan, Y.; Yao, S., Recent Advances in Electrochemical Glucose Biosensors: a Review. *RSC Adv* **2013**, 3, 4473-4491.

6. Haghighi, B.; Tabrizi, M. A., Direct Electron Transfer from Glucose Oxidase Immobilized on an Overoxidized Polypyrrole Film Decorated with Au Nanoparticles. *Colloids Surf B* **2013**, 103, 566-571.

7. Wang, J. J.; Myung, N. V.; Yun, M. H.; Monbouquette, H. G., Glucose Oxidase Entrapped in Polypyrrole on High-Surface-Area Pt EElectrodes: a Model Platform for Sensitive Electroenzymatic Biosensors. *J Electroanal Chem* **2005**, *575*, 139-146.

8. Saiki, R. K.; Scharf, S.; Faloona, F.; Mullis, K. B.; Horn, G. T.; Erlich, H. A.; Arnheim, N., Enzymatic Amplification of Beta-Globin Genomic Sequences and Restriction Site Analysis for Diagnosis of Sickle-Cell Anemia. *Science* **1985**, 230, 1350-1354.

9. Saiki, R. K.; Gelfand, D. H.; Stoffel, S.; Scharf, S. J.; Higuchi, R.; Horn, G. T.; Mullis, K. B.; Erlich, H. A., Primer-Directed Enzymatic Amplification of DNA with a Thermostable DNA-Polymerase. *Science* **1988**, 239, 487-491.

10. Byun, K.-E.; Choi, D. S.; Kim, E.; Seo, D. H.; Yang, H.; Seo, S.; Hong, S., Graphene–Polymer Hybrid Nanostructure-Based Bioenergy Storage Device for Real-Time Control of Biological Motor Activity. *ACS Nano* **2011**, 5, 8656-8664.

11. Lee, D. J.; Kim, E.; Kim, D.; Park, J.; Hong, S., Nano-Storage Wires. *ACS Nano* **2013**, 7, 6906-6913.

12. Burgmayer, P.; Murray, R. W.; An Ion Gate Membrane: Electrochemical Control of Ion Permeability through a Membrane with an Embedded Electrode. *J Am Chem Soc* **1982**, 104, 6139-6140.

13. Kost, J.; Langer, R.; Responsive Polymeric Delivery Systems. *Adv Drug Delivery Rev* **2012**, 64, 327-341.

14. Kontturi, K.; Pentti, P.; Sundholm, G., Polypyrrole as a Model

Membrane for Drug Delivery. *J Electroanal Chem* **1998**, 453, 231-238.

15. Mattos, C.; Ringe, D., Proteins in Organic Solvents. *Curr Opin Struct Biol* **2001**, 11, 761-764.

16. Knubovets, T.; Osterhout, J. J.; Klibanov, A. M., Structure of Lysozyme Dissolved in Neat Organic Solvents as Assessed by NMR and CD Spectroscopies. *Biotechnol Bioeng* **1999**, 63, 242-248.

17. Lopez Cascales, J. J.; Otero, T. F. Molecular Dynamic Simulation of the Hydration and Diffusion of Chloride Ions from Bulk Water to Polypyrrole Matrix. *J Chem Phys* **2004**, 120, 1951–1957.

18. Lopez Cascales, J. J.; Fernandez, A. J.; Otero, T. F. Characterization of the Reduced and Oxidized Polypyrrole/Water Interface: A Molecular Dynamics Simulation Study. *J Phys Chem B* **2003**, 107, 9339–9343.

19. Smela, E., Conjugated Polymer Actuators for Biomedical Applications. *Adv Mat* **2003**, 15, 481-494.

20. Smela, E.; Gadegaard, N., Volume Change in Polypyrrole Studied by Atomic Force Microscopy. *J Phys Chem B* **2001**, 105, 9395-9405.

21. Suárez, M. F.; Compton, R. G., In situ Atomic Force Microscopy Study of Polypyrrole Synthesis and the Volume Changes Induced by Oxidation and Reduction of the Polymer. *J Electroanal Chem.* **1999**, 462, 211-221.

22. Clark, L. C.; Lyons, C., Electrode Systems for Continuous

Monitoring in Cardiovascular Surgery. *Ann Ny Acad Sci* **1962**, 102, 29-45.

23. Zhou, Y.; Lachman, N.; Ghaffari, M.; Xu, H. P.; Bhattacharya, D.; Fattahi, P.; Abidian, M. R.; Wu, S.; Gleason, K. K.; Wardle, B. L.; Zhang, Q. M., A High Performance Hybrid Asymmetric Supercapacitor via Nano-scale Morphology Control of Graphene, Conducting Polymer, and Carbon Nanotube Electrodes. *J Mater Chem A* **2014**, 2, 9964-9969.

24. Zhou, M. J.; Diwu, Z. J.; PanchukVoloshina, N.; Haugland, R. P., A Stable Nonfluorescent Derivative of Resorufin for the Fluorometric Determination of Trace Hydrogen Peroxide: Applications in Detecting the Activity of Phagocyte NADPH Oxidase and Other Oxidases. *Anal Biochem* **1997**, 253, 162-168.

25. Otero, T. F.; Costa, S. O.; Ariza, M. J.; Marquez, M., Electrodeposition of Cu on Deeply Reduced Polypyrrole Electrodes at Very High Cathodic Potentials. *J Mater Chem* **2005**, 15, 1662-1667.

26. Zhao, Y. C.; Zhan, L.; Tian, J. N.; Nie, S. L.; Ning, Z., Enhanced Electrocatalytic Oxidation of Methanol on Pd/Polypyrrole-Graphene in Alkaline Mmedium. *Electrochim Acta* **2011**, 56, 1967-1972.

27. Buxton, G. V.; Greenstock, C. L.; Helman, W. P.; Ross, A. B., Critical Review of Rate Constants for Reactions of Hydrated Electrons, Hydrogen Atoms and Hydroxyl Radicals ·OH/·O−. in Aqueous Solution. *J Phys Chem Ref Data* **1988**, 17, 513-886.

28. WOOD, P. M., The Potential Diagram for Oxygen at pH 7. *Biochem J* **1988**, 253, 287-289.

Chapter 5

Conclusion

In this dissertation, we developed a MBS that could recognize various odorants and tastants indicating the food contaminations. We showed that the MBS could monitor the responses of various sensory receptors, which indicated different binding characteristics. The MBS represented a human-like performance in a mixture solution with 1 pM detection limit for their target molecules. Furthermore, the MBS could detect food contamination indicators from the real food samples *via* the combinations of responses of various receptors.

In the second, a ONBN for the detection of CV was successfully developed *via* the hybridization of NDs containing TAAR13c receptors produced in *E. coli*. and CNT-FET with the floating electrodes. The well-developed ONBN could mimic native binding pockets and their responses to recognize CV with high sensitivity and selectivity. The immobilized T13NDs on floating electrodes *via* linker molecules with the orientation enabled ONBN to discriminate target molecules with human-like sensitivity and selectivity. Moreover, an ONBN quantitatively rocognize CV in real food samples by spoilage periods.

These results showed that our ONBN platform based on GPCR-conjugated FET could provide a novel platform for the detection of death-associated odor and have a potential on practical bioelectronic sensor applications.

Lastly, in the last part of this dissertation, we discussed the novel strategy to control the enzymatic reaction *via* nanostructured conducting polymer. Using this strategy, we controlled the enzymatic reaction in real-time using electrical stimuli. The fabricated BSC structures showed the switch of enzymatic reaction in real-time. The BSC structure resulted in the 20-folds increased glucose oxidation reaction by the introduction of a negative bias voltage on BSC than that without a bias voltage. Moreover, we controlled the enzymatic reaction on specific regions using the BSC since that could be developed on specific regions. In consideration of the fact that enzymes enable useful and versatile to bio-chemical reactions, the capability to control the enzymatic reactions using simple electrical signals could open up various applications in the field of biochips and biochemical industries.

Chapter 6

Abstract in Korean

초록

나노물질들을 기반으로 제작된 인공감각 센서는 그들이 갖는 매우 뛰어난 감도와 선택성 때문에 많은 관심을 받고 있다. 동물들의 감각기관에 대한 기본적인 연구와 나노물질과 바이오물질과의 융합은 높은 성능을 갖는 센서의 제작에 필수적인 요소라고 할 수 있다.
본 연구에서는 다양한 감각 수용체 단백질의 반응성에 대한 연구를 진행하였다. 이를 위해서 우리는 동물의 감각기관의 반응성을 모사하여 음식물의 부패를 검지할 수 있는 신뢰도 높은 인공감각기관을 개발하고자 하였다.
먼저, 이를 위해서 우리는 다양한 부패물질을 검지가능한 다채널을 갖는 인공감각 센서를 개발하였다. 우리는 개발한 다채널 센서를 이용하여 여러가지 감각 수용체 단백질의 다양한 반응 특성을 살펴보았다. 다채널 센서는 다양한 타겟 물질에 대해서 1 pM의 매우 높은 수준의 감도를 보여주었다. 게다가, 이 센서를 이용하여 실제 부패한 음식에서의 다양한 반응을 살펴볼 수 있었고, 이들의 반응의 조합을 통해서 실제 사람과 같은 반응을 나타내는 것을 확인할 수 있었다.
다음으로는 방향성과 높은 안정성을 갖는 나노디스크 기반의 단백질 부패 검지센서를 개발하였다. 수용체 단백질이 포함된 나노디스크를 탄소나노튜브 기반 소자의 플로팅 전극 부분에 방향성을 갖게끔 고정화하여, 높은 감도와 높은 선택성을 갖게끔 유도하였다. 또한,

나노디스크 기반의 단백질 부패 검지센서는 실제 음식의 단백질 부패도를 부패한 기간에 따라서 정량적으로 분석할 수 있었다.
위와 같은 결과들은 우리의 수용체 단백질 기반의 인공감각기관에 대한 연구가 다양한 식품개발과 의료진단에 응용될 수 있다는 것을 보여준다. 뿐만 아니라, 실제와 같은 반응을 모사할 수 있는 감각기관 개발에 기여할 수 있다는 것을 보여준다.
본 연구의 마지막 부분에서는 전도성 고분자 물질의 나노구조를 이용하여, 효소반응을 조절하기 위한 연구에 대해서 언급하였다. 바이오 스위치칩이라 명명한 해당 기술은 전기적 자극을 통해서 효소의 작용을 전기적 자극이 없을 때와 대비하여 20배 가량 향상시킬 수 있다는 것을 보여준다. 뿐만 아니라, 우리는 바이오 스위치칩을 우리가 원하는 부분에만 형성시킬 수 있다는 점을 활용한다면, 원하는 부분의 효소작용만을 조절할 수 있다는 점을 보여준다. 효소 단백질이 갖는 유용성과 다양한 응용 분야를 생각해봤을 때, 본 연구는 다양한 바이오칩 및 생화학연구분야에 많은 기여를 할 수 있을 것이라고 보여진다.

주요어 : 인공감각기관, 음식물 부패도, 수용체, 나노디스크, 탄소나노튜브
학번 : 2011-24029